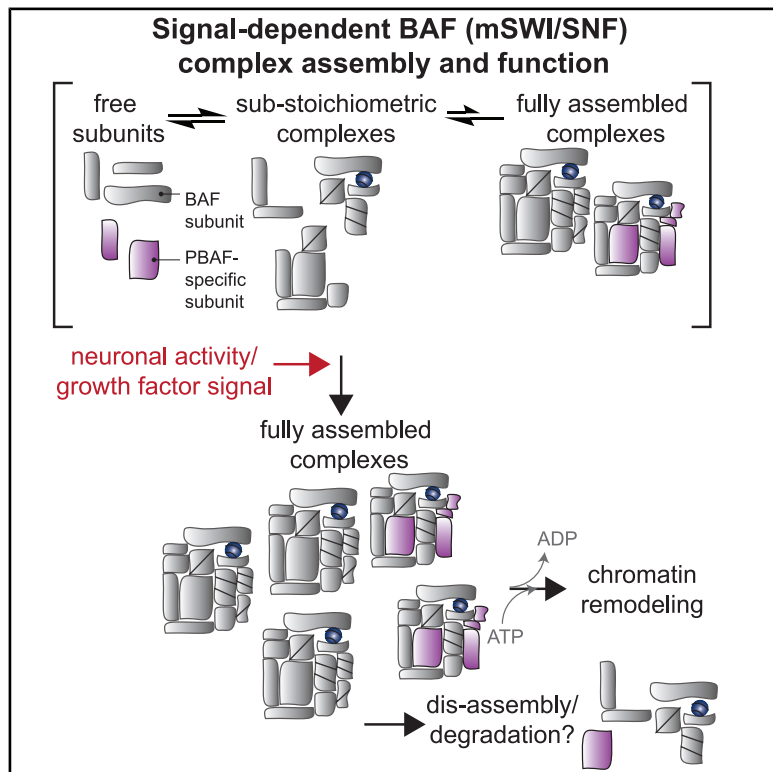


Synaptic activity causes minute-scale changes in BAF complex composition and function

Graphical abstract



Authors

Sai Gourisankar, Sabin A. Nettles,
Wendy Wenderski, ..., Hind Z. Abuzaid,
Steven P. Gygi, Gerald R. Crabtree

Correspondence

crabtree@stanford.edu

In brief

Gourisankar et al. discover that signals at the cell membrane rapidly reprogram the composition of chromatin remodeling complexes in the nucleus. In neurons, dynamic assembly helps translate synaptic activity into targeted changes in chromatin accessibility, revealing a key mechanism by which excitatory stimuli shape gene regulation to facilitate neuronal plasticity.

Highlights

- Signals at the membrane trigger BAF and PBAF complex assembly in under 15 min
- BAF/PBAF opens chromatin at 10% of neuronal activity-responsive elements
- Neuronal activity triggers subunit phosphorylation and directs remodeling



Article

Synaptic activity causes minute-scale changes in BAF complex composition and function

Sai Gourisankar,^{1,3,5} Sabin A. Nettles,^{1,5} Wendy Wenderski,^{1,2} Joao A. Paulo,⁴ Sam H. Kim,¹ Kyra C. Roepke,¹ Claire Ellis,¹ Hind Z. Abuzaid,¹ Steven P. Gygi,⁴ and Gerald R. Crabtree^{1,2,6,*}

¹Department of Pathology, Stanford University School of Medicine, Stanford, CA 94305, USA

²Department of Developmental Biology, Stanford University School of Medicine, Stanford, CA 94305, USA

³Department of Chemical Engineering, Stanford University, Stanford, CA 94305, USA

⁴Department of Cell Biology, Harvard Medical School, Boston, MA 02115, USA

⁵These authors contributed equally

⁶Lead contact

*Correspondence: crabtree@stanford.edu

<https://doi.org/10.1016/j.molcel.2025.05.017>

SUMMARY

Genes encoding subunits of the BAF ATP-dependent chromatin remodeling complex are among the most enriched for deleterious *de novo* mutations in intellectual disabilities and autism spectrum disorder, but the causative molecular pathways are not understood. Synaptic activity in neurons is critical for learning, memory, and proper neural development. While BAF is required for activity-dependent developmental processes, such as dendritic outgrowth, the immediate molecular consequences of neuronal activity on BAF complexes are unknown. Here, we report that neuronal activity induces dramatic remodeling of the subunit composition of BAF complexes within 15 min, concurrent with both phosphorylation and dephosphorylation of its subunits. These biochemical effects are a convergent phenomenon downstream of multiple calcium-activated signaling pathways in mouse neurons and mouse fibroblasts and correspond to changes in BAF-dependent chromatin accessibility. Our studies imply that BAF decodes signals at the membrane by altering the combinatorial composition of its subunits.

INTRODUCTION

Adenosine triphosphate (ATP)-dependent chromatin remodelers facilitate transcription factor (TF) binding and activity by regulating the accessible chromatin landscape through evicting, translocating, and remodeling nucleosomes.¹ Genes encoding remodelers are among the most highly mutated in neurodevelopmental disorders such as intellectual disabilities and autism spectrum disorder.² Subunits of the BAF (Brg1/Brm-associated factor) complex, also called mammalian SWI/SNF (mSWI/SNF), are particularly enriched in *de novo* mutations in these disorders, implicating them as likely causative.^{2,3} Recently, recessive mutations in neuronal BAF complexes were shown to be causative in autism.⁴ Moreover, variants in the gene *PBRM1* (BAF180), a polybromo-associated BAF (PBAF)-specific subunit, have been implicated in increased intelligence, cognition, and higher educational attainment in genome-wide association studies.⁵⁻⁷

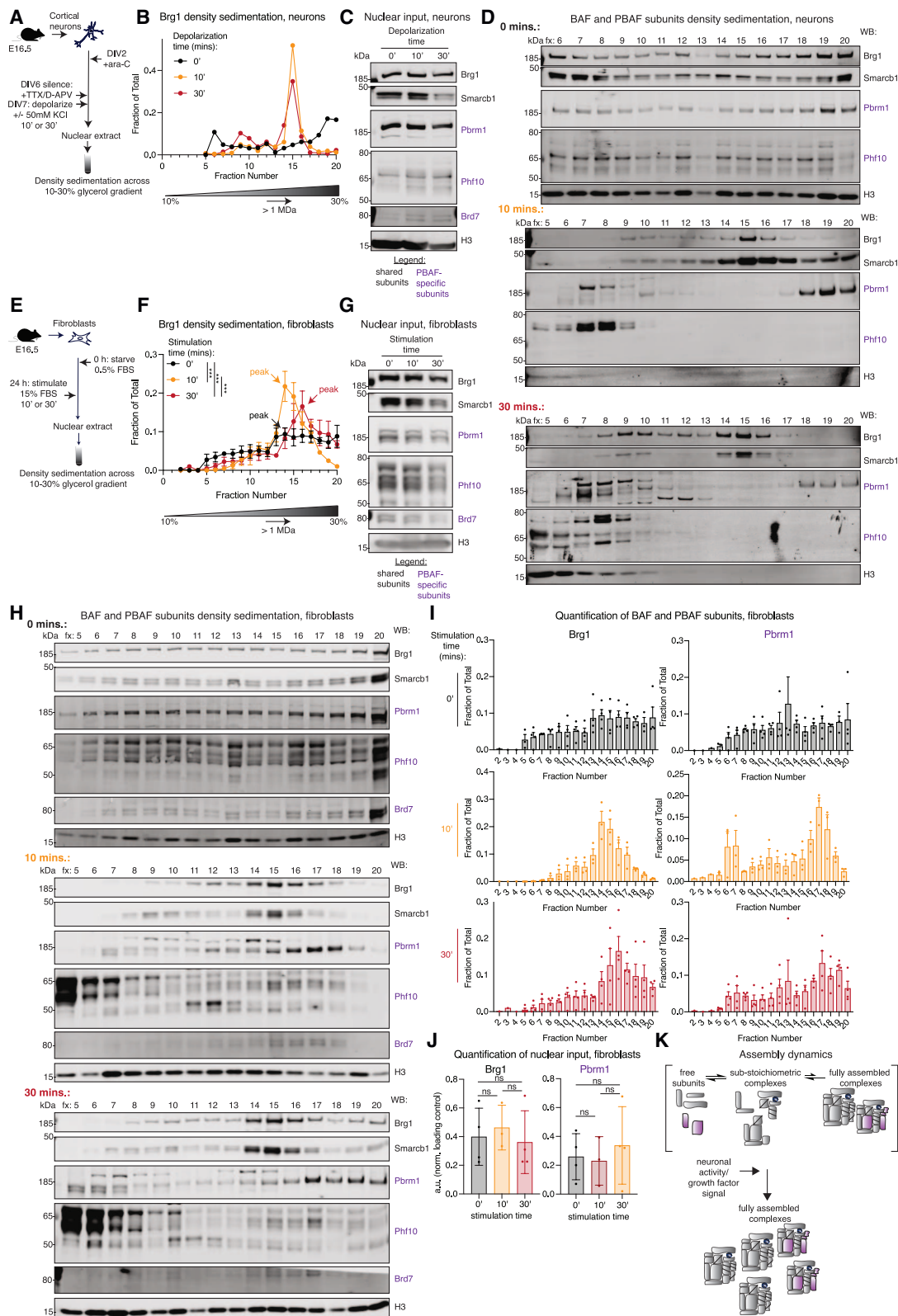
Synaptic activity in neurons leads to immediate *de novo* transcription of genes responsible for shaping social behavior, learning, and memory.⁸ Activity-dependent biochemical regulation of many chromatin modifiers and TFs facilitates the transcriptional response to neuronal activity.⁹⁻¹⁴ While BAF complexes are critical to activity-dependent neuronal processes

such as dendritic arborization,^{15,16} the direct molecular consequences of synaptic activity on BAF complexes are unknown.

BAF complexes are macromolecular machines assembled combinatorially from 15 different subunits encoded by 29 different genes.^{17,18} At least three main classes of mammalian BAF complexes are present in all cells: canonical BAF (cBAF), polybromo-associated BAF (PBAF), and non-canonical BAF (ncBAF), each containing one of the two paralogous ATPases (BRG1 or BRM) and class-specific, non-redundant subunits.^{18,19} For example, PBAF is defined by replacement of subunit ARID1A/B (BAF250A/B) with ARID2 (BAF200) and BAF45B/C/D with PHF10 (BAF45A) and by the inclusion of PBRM1 (BAF180) and BRD7. In total, PBAF is larger than cBAF by almost 0.5 MDa.^{17,18} Combinatorial selection of subunits gives the assemblies a cell-type and functional specificity.^{17,20}

The formation of diverse protein interaction surfaces on BAF complexes alters interactions with TFs, directs localization and activity on chromatin, and guides biologic processes. For example, during neural development, the neural progenitor-specific BAF subunits, ACLT6A (BAF53A) and SS18, are replaced by neuron-specific subunits, ACLT6B (BAF53B) and SS18L (CREST), respectively,²¹ in a switch orchestrated by microRNAs miR-9 and miR-124.^{21,22} Postmitotic neurons have a specialized neuronal BAF complex that is critical for neuronal function.^{15,16}





(legend on next page)

Here, we map the direct molecular effects of signals at the membrane on BAF complexes in the nucleus. We discover that BAF and PBAF subunits are present in an equilibrium of three states in resting cells: assembled complexes, partially assembled complexes, and unassembled subunits. Synaptic activity in neurons or growth factor signaling in fibroblasts prompts a rapid (after 10 min) shift in the equilibrium to assembled complexes. The compositional change is concurrent with function on chromatin; more than 10% of activity-responsive DNA elements require BAF/PBAF ATPase function for producing accessibility. We found evidence that PBAF assembly contributes to opening at these elements. Moreover, subunits are rapidly hyper- and hypo-phosphorylated. Hyper-phosphorylation of SmarcC2 (Baf170), a core subunit required for assembly of all BAF complexes, is dispensable for assembly but sufficient to redirect BAF activity on chromatin and to reprogram gene expression. Our time-resolved biochemical and genomic experiments indicate that BAF complexes are remarkably dynamic in both composition and function, with implications for studies of signal-dependent gene regulation.

RESULTS

Signal-dependent BAF complex assembly in neurons and fibroblasts

To examine the direct consequences of synaptic activity on BAF complex assembly, we examined the nuclei isolated from primary cortical neurons cultured *in vitro* for 7 days^{4,23} from embryonic day 16.5 (E16.5) mice (Figure 1A). Neuronal activity was mimicked in culture by depolarization with 50 mM potassium chloride to stimulate calcium influx through L-type voltage-sensitive calcium channels, and it leads to rapid expression of activity-dependent genes such as c-Fos.^{23,24} Separation of native soluble nuclear proteins by sedimentation through a 10%–30% glycerol gradient revealed that 10 min of depolarization causes a sharp peak of the ATPase subunit Brg1 to form in fractions 13–16 (Figure 1B). This corresponds to a ~1-MDa complex.¹⁶ In neurons silenced with the sodium channel blocker tetrodotoxin (TTX) and the N-methyl-D-aspartate (NMDA) receptor antagonist D-2-amino-5-phosphonovaleric acid (D-APV), Brg1 was present almost uniformly across the gradient, indicating that only a fraction of total Brg1 is assembled into larger complexes in resting neurons (Figure 1B). The total levels of most

nuclear BAF and PBAF subunits changed minimally after 10 min, except for SmarcB1 (Baf47) and Brg1, which decreased modestly after 30 min of depolarization (Figure 1C). Brg1 co-localized with the pan-BAF subunit SmarcB1 (Figure 1D), indicating that the dynamics of Brg1 complex incorporation observed represent assembly of BAF complexes. Indeed, depolarization prompted rapid assembly of both BAF and PBAF, as evidenced by sharp localization peaks at higher-molecular-weight fractions in their respective subunits after 10 and 30 min (Figure 1D). To validate our findings, we evaluated BAF complex assembly using an alternate nuclear extraction protocol by preparing extracts using a physiological-salt (150 mM NaCl) buffer supplemented with benzonase.^{25,26} Separation of complexes by glycerol gradient after 30 min of depolarization showed comparable assembly dynamics (Figures S1A–S1C). Of note, the reduced enrichment of PBAF subunits in 150 mM NaCl-extracted nuclear protein, compared with extraction using ammonium sulfate (used at 0.4 M, STAR Methods), is consistent with studies showing that PBAF has a higher affinity for chromatin.²⁷ Thus, membrane signaling prompts the assembly of BAF and PBAF complexes inside the nucleus of a living cell.

To determine if the signaling-directed assembly of BAF complexes occurs in other cell types, we examined BAF complexes in mouse embryonic fibroblasts (MEFs) that had been serum-starved or exposed to serum for 0, 10, or 30 min (Figure 1E). Quiescent fibroblasts respond to growth factors through calcium influx and mitogen-activated protein kinase (MAPK) signaling by rapidly inducing gene transcription²⁸ with similar kinetics as in neurons.^{12,13} Separation of complexes by glycerol gradient sedimentation revealed that 10 min of stimulation causes Brg1 to accumulate preferentially in a broad peak around fraction 14 (Figure 1F). As in neurons, Brg1 was distributed in assembled and un-assembled complexes in quiescent fibroblasts; only ~70% of Brg1 was incorporated in >~1-MDa complexes in resting fibroblasts (Figure 1F). Not only did stimulation in fibroblasts assemble Brg1 into BAF complexes, but it also significantly ($p < 0.0001$) shifted the Brg1 distribution to higher fractions, overlapping with PBAF-specific subunits with time (10–30 min of stimulation) (Figure 1F). This indicated the incorporation of Brg1 into PBAF and suggested that stimulation may change the relative stoichiometry of fully assembled PBAF:BAF complexes. Changes in total BAF and PBAF subunit levels in the nucleus mirrored those in neurons, with little change at 10 min and a modest decrease in

Figure 1. Signal-dependent BAF complex assembly in neurons and fibroblasts

- (A) Schematic of glycerol gradient experiment in neurons with or without depolarization to model neuronal activity. DIV, day *in vitro*.
 - (B) Quantification of Brg1 protein levels across gradient fractions in neurons.
 - (C) Protein levels of BAF and PBAF subunits in inputs to gradient in neurons.
 - (D) Protein levels of subunits across gradients in neurons. Experiments in (B)–(D) are representative of two technical replicates (10') or two biological replicates (0' and 30').
 - (E) Schematic of gradient experiment in fibroblasts with or without serum stimulation to model growth factor signaling.
 - (F) Quantification of Brg1 protein levels across gradient fractions in fibroblasts; mean \pm SEM; *** $p < 0.001$; significance computed by two-sample Wasserstein distance test between distributions.
 - (G) Protein levels of BAF and PBAF subunits in inputs to gradient in fibroblasts.
 - (H) Protein levels of subunits across gradients in fibroblasts.
 - (I) Quantification of subunits across gradient in fibroblasts; mean \pm SEM; Brg1 is reproduced from (F) for comparison.
 - (J) Quantification of subunits in inputs to gradients in fibroblasts; mean \pm SD. Experiments in (F)–(J) quantify or are representative of three (10') or four (0' and 30') biological replicates.
 - (K) Model of BAF complex assembly dynamics observed.
- See also Figure S1 and Data S1.

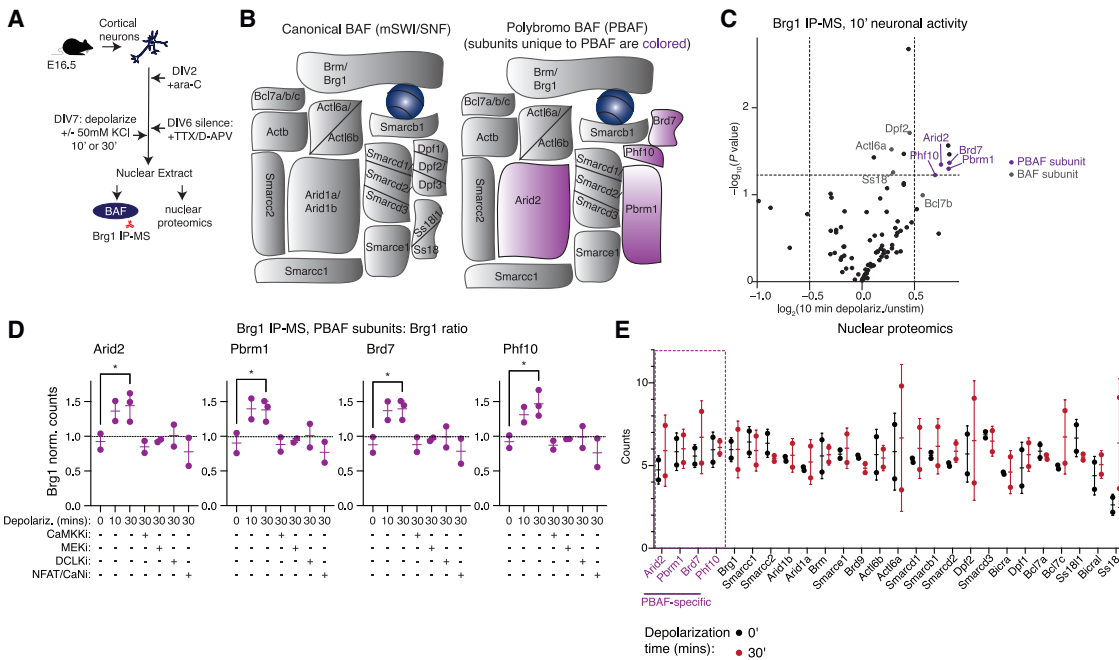


Figure 2. Neuronal activity assembles and stabilizes PBAF complexes

(A) Schematic of IP-MS and nuclear proteomics experiment in neurons with or without depolarization to model neuronal activity; anti-Brg1 antibody used for IP (STAR Methods). DIV, day *in vitro*.

(B) Schematic of BAF and PBAF complexes.

(C) Differential proteins ($p \leq 0.05$ and \log_2 fold change ≥ 0.5 or ≤ -0.5) enriched with Brg1 IP after 10 min of neuronal activity; two biological replicates; p values computed by two-sided unpaired t test.

(D) Enrichment of PBAF-specific subunits after Brg1 IP, normalized to bait (Brg1), after 10 or 30 min of neuronal activity and/or inhibition of calcium-activated signaling; inhibitors used were CaMKKi: STO-609, 3 μ M; MEKi: PDO325901, 3 μ M; DCLKi: DCLK-IN-1, 2.5 μ M; NFAT/CaNi: 10 nM FK506 + 1 μ M cyclosporin A (CsA); cyclosporin A and FK506 were used together because of the greater abundance of calcineurin in neurons, compared with FKBP (FK506-binding protein) and cyclophilin, which are required for formation of inhibitor complexes³⁰; mean \pm SD, 2–3 biological replicates; *p* values computed by two-sided one-way ANOVAs between the mean of 0' and means of 10' or 30' only; **p* \leq 0.05; for other BAF subunits, see Figure S2G.

(E) Total levels of all BAF subunits in whole nuclear extracts from neurons; mean \pm SD, two biological replicates.

See also Figure S2 and Tables S1 and S2.

Smarcb1 and Brg1 at 30 min (Figures 1G and 1J). Smarcb1 dynamics mirrored Brg1 indicating, as in neurons, the formation of BAF complexes (Figure 1H). Consistent with the relative sizes of cBAF complexes (~1 MDa) and PBAF complexes (~1.5 MDa),^{17,18} PBAF-specific subunits Pbrm1 (Baf180), Phf10 (Baf45a), and Brd7 separated preferentially into higher-molecular-weight fractions and assembled into complexes as a result of stimulation (Figure 1H). Quantification of the changes in BAF and PBAF distributions with time indicated that both categories of complexes assemble within 30 min without significant changes in total subunit protein levels (Figures 1I and 1J).

Altogether, our gradient analyses reveal that BAF subunits in quiescent mitotic and postmitotic cells are maintained in an equilibrium between three relative states: assembled complexes, unassembled sub-stoichiometric sub-complexes, and individual subunits (Figure 1K). Signals from the membrane prompt a shift toward assembled complexes.

Activity assembles and stabilizes PBAF

To directly probe the effects of neuronal activity on BAF complex subunit composition, we immunoprecipitated BAF complexes with an antibody specific to Brøn, which is approximately 2.2-

fold more abundant in embryonic neuronal nuclear extract than its homolog Brm (Table S1), after 10 or 30 min of depolarization (Figure 2A and Figures S2A–S2F). Proteomic analysis identified 1,637 uniquely interacting proteins with Brg1 of which 1,452 had more than one peptide quantified, including all possible BAF subunits (Table S2). Quantification of BAF subunit recovery during each step of our extraction protocol indicated that the input to the mass spectrometer contained ~90% of all BAF complexes in the cell (Figure S2A). PBAF complexes incorporate four complex-specific subunits²⁹: Arid2, Pbrm1, Phf10, and Brd7 (Figure 2B). All four PBAF-specific subunits (Figure 2B) were significantly enriched (p value ≤ 0.05 and \log_2 fold change > 0.5) in immunoprecipitated elutes after 10 min of depolarization (Figure 2C). Normalization to bait (i.e., Brg1) indicated that all four subunits increased their interaction with Brg1 by a comparable magnitude (50%) (Figure 2D). There was no change in enrichment of most of the other subunits that are common to all BAF complexes such as Smarcc2 (Baf170), Smarcb1, or Smarce1 (Baf57), except for Dpf1 (Baf45b), which showed reduced association to Brg1 by 20% (Figure S2G). Dpf1 (Baf45b) is a paralog of Phf10 (Baf45a) that is mutually exclusive in the BAF complex.¹⁸ The decrease in Dpf1 could reflect

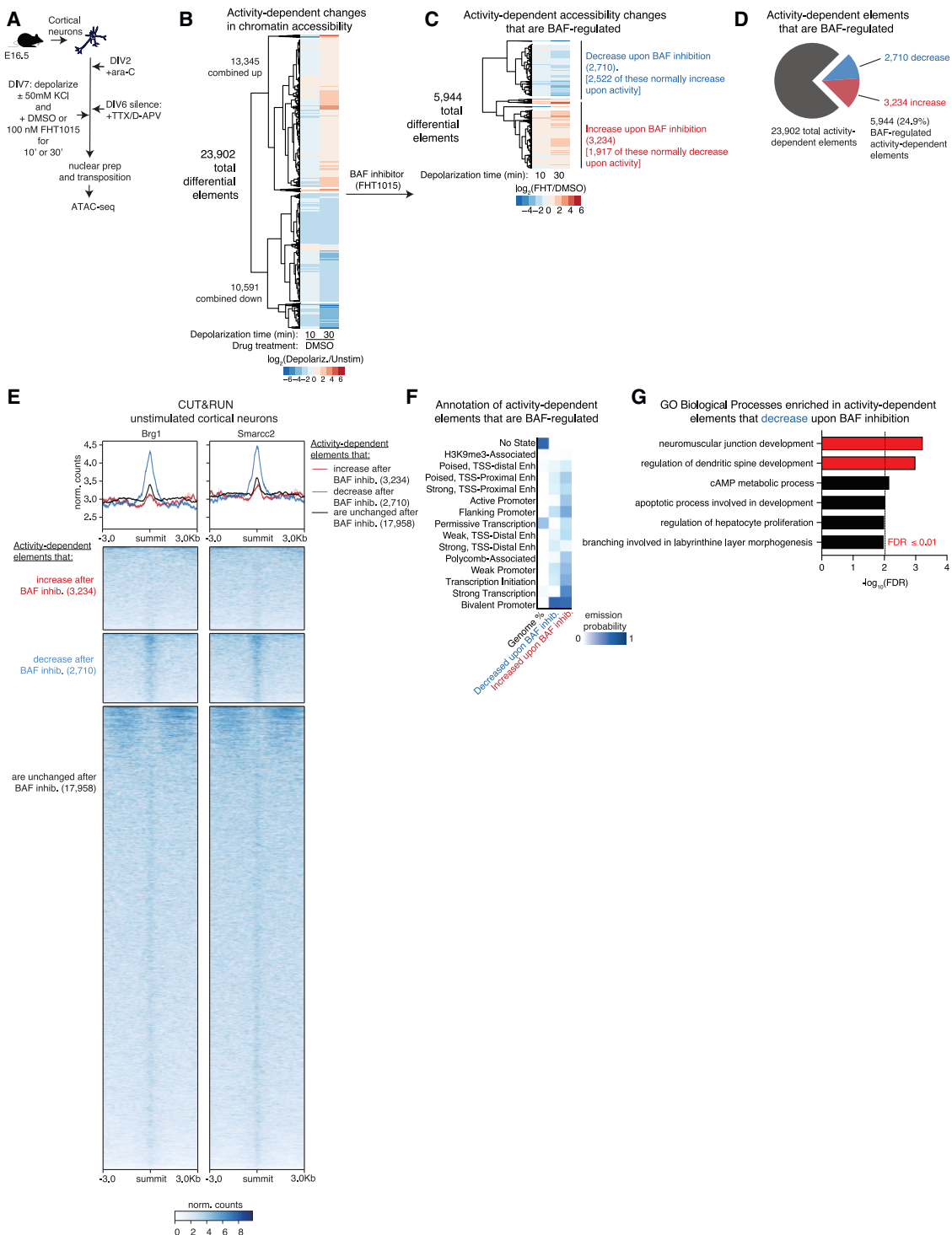


Figure 3. BAF regulates 25% of neuronal activity-dependent chromatin

(A) Schematic ATAC-seq in neurons with or without depolarization to model neuronal activity and/or BAF ATPase inhibition (FHT1015, 100 nM). DIV, day *in vitro*. (B) All DNA elements that show activity-dependent changes in chromatin accessibility (adj. $p \leq 0.05$ and \log_2 fold change ≥ 1 or ≤ -1). (C) Only activity-dependent elements that changed significantly (adj. $p \leq 0.05$) upon BAF inhibition. For (B) and (C): two biological replicates; p values were computed by two-sided Wald test and adjusted for multiple hypotheses by Benjamini-Hochberg. (D) Proportion of all activity-dependent elements that are regulated by BAF.

(legend continued on next page)

stabilization of PBAF at the expense of other types of BAF complexes. The total protein levels of most BAF subunits did not change significantly with depolarization, but biological variability was observed (Figures 2E and S2D). Concurrent with stoichiometry changes with respect to Brg1, PBAF complex formation in neurons, as assessed by gradient separation of Pbrm1, peaked at 10 min and appeared to disassemble after 30 min of depolarization (Figures 1D and S1D). This result is consistent with our immunoprecipitation coupled with mass spectrometry (IP-MS) analyses that show that PBAF subunits increase their interaction with Brg1 after 10 min of depolarization (Figure 2C). It also suggests that prolonged signaling triggers a disassembly pathway to regenerate BAF complexes or switch functions on chromatin.

Calcium influx in neurons activates multiple membrane-to-nucleus signaling pathways including MAPK signaling,^{31,32} calcium/calmodulin-dependent kinase signaling (CaMK),^{33–36} double-cortin-like kinase signaling (DCLK),^{37,38} and calcineurin (CaN)-nuclear factor of activated T cell (NFAT) signaling.^{30,39} Each might produce biochemical modifications on BAF subunits that mediate assembly. To examine this, we blocked each signaling cascade by treating neuronal cultures with MAPK/ERK kinase (MEK), calcium/calmodulin-dependent protein kinase kinase (CaMKK), DCLK, or CaN inhibitors, respectively, and assessed proteins enriched after Brg1 IP (Figures 2D and S2C). Blockade of any one of the calcium-activated kinase cascades reversed the enrichment of PBAF subunits with Brg1 (Figure 2D). This result raises the possibility that the increase in PBAF:Brg1 stoichiometry is a convergent effect of multiple membrane-to-nucleus signaling cascades. Taken together, our biochemical analyses suggest that signaling at the membrane results in rapid alteration in complex assembly and may trigger the formation of PBAF complexes (or an intermediate in their formation) while stabilizing PBAF complexes containing Brg1. However, our results do not rigorously exclude the rapid formation of an alternative assembly only partially related to well-characterized PBAF complexes.

BAF regulates 25% of activity-dependent chromatin

We hypothesized that activity-induced BAF complex assembly would mediate its remodeling functions on chromatin. To investigate activity-dependent changes in chromatin facilitated by BAF, we began by identifying DNA elements that are the direct targets of BAF downstream of neuronal activity. We built an atlas of changes in accessible chromatin by assay for transposase-accessible chromatin with sequencing (ATAC-seq) in neurons after acute (10 or 30 min) membrane depolarization and addition of a specific Brg1/Brm ATPase inhibitor, FHT1015 (Figures 3A and S3A). Neuronal activity significantly changed accessibility by more than 2-fold (adj. $p \leq 0.05$) at 23,902 elements (Figure 3B). These elements represent activity-dependent chromatin. BAF

inhibition caused approximately 25% ($n = 5,944$) of these activity-dependent elements to significantly change (adj. $p \leq 0.05$) (Figures 3C and 3D). Notably, 11.3% ($n = 2,710$) of activity-dependent elements lost accessibility after BAF inhibition; ordinarily, most of these (93%) would have been opened after neuronal activity (Figure 3C, top). Hence, BAF ATPase function is required for neuronal activity to open chromatin at 10.5% of activity-responsive elements.

Changes in chromatin accessibility were detected within 10 min of ATPase inhibition (Figure S3B), consistent with recent studies of acute BAF inhibition or degradation in mouse embryonic stem cells (mESCs),^{41,42} suggesting that BAF may be poised on chromatin to initiate remodeling activity. Indeed, cleavage under targets and release using nuclease (CUT&RUN) in resting cortical neurons showed enrichment of Brg1 and Smarcc2 at activity-dependent elements that lost accessibility after BAF inhibition (Figure 3E), indicating that BAF was poised to facilitate an activity-dependent response on chromatin 10 min after receiving a signal at the membrane. Activity-dependent elements that gained accessibility after BAF inhibition had comparatively little enrichment of Brg1/Smarcc2 (Figure 3E), suggesting that accessibility changes at these elements are indirect targets of BAF ATPase function.

Chromatin opened by BAF after neuronal activity occurred preferentially at genes responsible for neuronal differentiation and cellular plasticity, as evidenced by two different region-to-function analyses. First, a hidden Markov model⁴³ trained on the epigenome of an E16.5 mouse forebrain⁴⁰ revealed that the elements dependent on both BAF and neuronal activity for opening are bivalent promoters characterized by H3K27me3 and H3K4me3 (Figure 3F). Bivalent domains maintain transcriptional plasticity of a locus by preparing them to be induced upon receipt of a developmental signal.⁴⁴ Second, region-to-gene linkage analysis⁴⁵ showed that these DNA elements regulate genes important for the development of neuromuscular junctions and dendritic spines (false discovery rate [FDR] ≤ 0.01) (Figure 3G). These results are consistent with neuronal BAF complexes being essential for activity-dependent dendritic arborization and activity-dependent synaptic plasticity.^{2,4} Combined, the CUT&RUN and ATAC-seq data identified the direct, neuronal activity-responsive targets of BAF complexes on chromatin.

PBAF directs activity-dependent chromatin opening

The DNA elements that require BAF ATPase function for activity-dependent opening were enriched (adj. $p \leq 0.0001$) for the X-box motif (Figures 4A and S3C). This is a 14-nt imperfect repeat sequence bound by the evolutionarily conserved regulatory factor binding to the X-box (RFX)-domain-containing TFs.^{46,47} Profiling the accessibility footprint at X-box motifs genome-wide showed that depolarization stimulated an increase in flanking accessibility

(E) Brg1 and Smarcc2 CUT&RUN in unstimulated neurons at summits of activity-dependent elements classified by their response to BAF inhibition from (C); signal merged from two biological replicates and normalized by sequence depth; plotted profile is mean \pm SEM.

(F) Enrichment of chromatin states in activity-dependent elements that require BAF ATPase function; chromatin-state hidden Markov model trained on E16.5 mouse forebrain epigenome in Gorkin et al.⁴⁰ Enh, enhancer; TSS, transcription start site.

(G) GO biological processes enriched in activity-dependent elements that require BAF ATPase function for opening; p values computed by Fisher's exact test and adjusted by Benjamini-Hochberg. cAMP, cyclic AMP.

See also Figure S3.

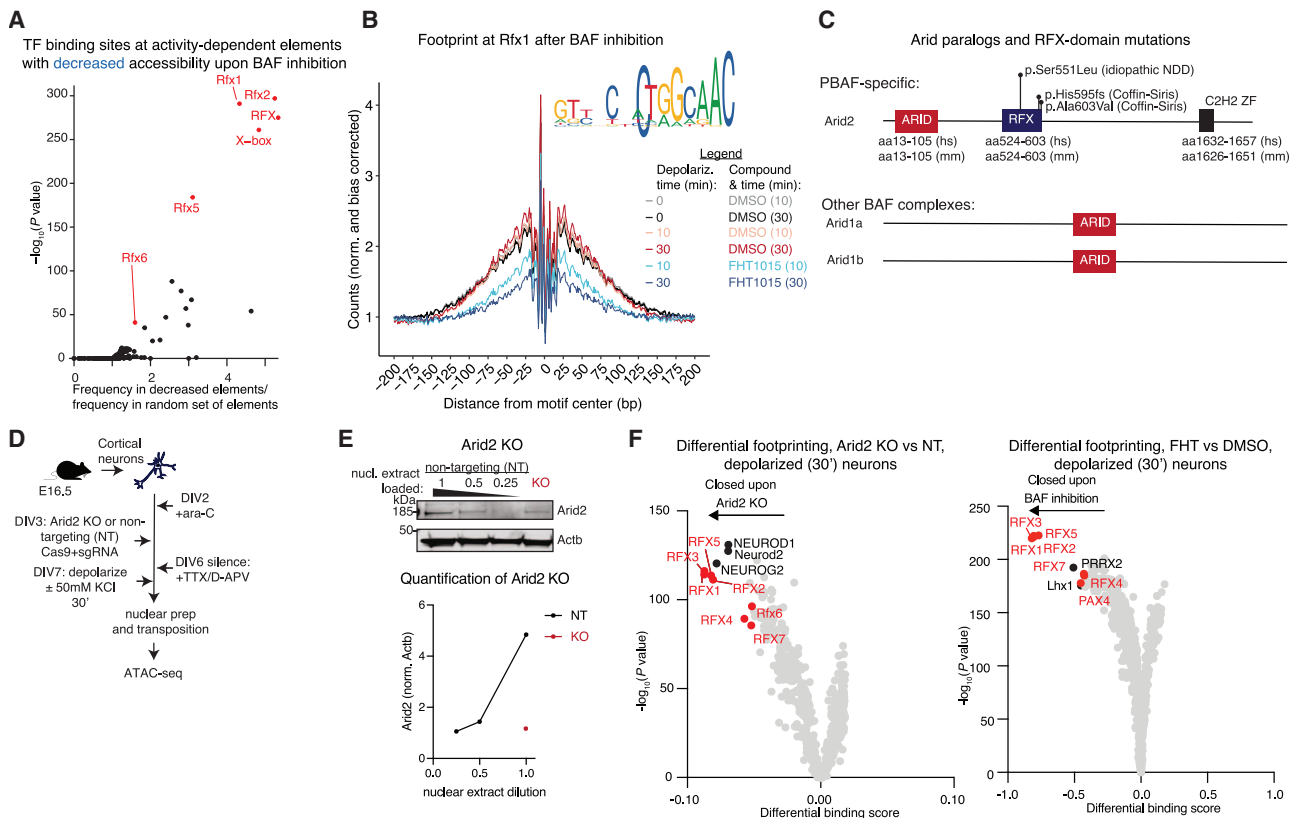


Figure 4. PBAF directs neuronal activity-dependent chromatin opening

(A) Enrichment of transcription factor (TF) motifs in neuronal activity-dependent elements that require BAF ATPase function for chromatin opening (these elements were defined in Figure 3C); p values computed by two-sided Fishers' exact test and adjusted by Benjamini-Hochberg, labeled in red: FDR < 0.05 .

(B) Footprint of accessibility at Rfx1 after neuronal activity and/or BAF inhibition.

(C) Comparison of Arid subunits in canonical BAF (cBAF) and PBAF complexes; *de novo* mutations in the RFX domain annotated (ClinVar). NDD, neurodevelopmental disorder; ZF, zinc finger; hs, *Homo sapiens*; mm, *Mus musculus*.

(D) Schematic of ATAC-seq in neurons with or without depolarization to model neuronal activity and/or CRISPR KO of Arid2; KO: Arid2 KO sgRNAs; NT: non-targeting sgRNA. DIV, day *in vitro*.

(E) Protein levels of Arid2 after KO or NT.

(F) Differential footprints of TF motifs after 30 min of activity in KO vs. NT (left) or BAF ATPase inhibitor vs. DMSO in wild-type neurons (from Figure 3C) (right); p values computed by two-sided t test of observed footprint change to mean of background footprint distribution.⁴⁹ For (A)–(F): two biological replicates. See also Figure S4 and Data S1.

that was dramatically lost upon BAF ATPase inhibition (Figure 4B). The losses in accessibility spanned ~ 300 bp centered on the motif, which is substantially larger than the average footprint of a human TF (16 bp).⁴⁸ This suggests that the footprint may reflect the remodeler and its activity.

We hypothesized that activity-induced assembly of PBAF (Figures 1 and 2) contributes to BAF chromatin remodeling activity via the introduction of RFX-DNA-binding capability in Arid2. Arid2 is specific to PBAF complexes and contains an RFX-DNA-binding domain as well as a C2H2 zinc finger (Figure 4C). Both DNA-binding domains are unique to Arid2 among the three paralogous BAF-complex Arids (Arid2, Arid1a, and Arid1b) and thus represent a unique characteristic of PBAF (Figure 4C). The Arid2 RFX domain shows sequence and structural homology to the DNA-binding domains of Rfx TFs (Figures S4A and S4B). In the yeast PBAF homolog, remodel the structure of chromatin (RSC),⁵⁰ the RFX domain is proximal to extra-nucleosomal linker

DNA (Figure S4C); the RSC complex itself binds both the nucleosome and exit DNA to occupy wide, ~ 150 - to 300-bp nucleosome-depleted regions.⁵¹ *ARID2* is a strong candidate Simons Foundation Autism Research Initiative (SFARI) autism risk gene, and *de novo* mutations in the human *ARID2* gene are implicated in idiopathic and Coffin-Siris syndrome-like intellectual disabilities,⁵² including those found in the RFX domain (Figure 4C), suggesting that it plays a biologic role in neurodevelopment.

To understand the contribution of PBAF to BAF-dependent and activity-dependent chromatin opening, we generated *Arid2* knockout (KO) neurons using lentiviral delivery of CRISPR-Cas9 and compared them with neurons infected with a non-targeting (NT) CRISPR-Cas9 single-guide RNA (sgRNA) (Figure 4D). We then assayed chromatin accessibility in KO and NT neurons from two independent mice before or after depolarization for 30 min (Figure 4D). Loss of Arid2 protein was incomplete ($\sim 70\%$ lost) likely due to the known long protein half-life of BAF subunits⁴ (Figure 4E).

Nevertheless, TF footprinting analysis using TOBIAS⁴⁹ demonstrated Arid2 KO significantly closed chromatin at X-box/Rfx motifs ($p < 10^{-100}$; adj. $p \leq 0.0001$), phenocopying the effect of BAF inhibition (Figure 4F). Loss of accessibility at X-box elements was greater than losses at any other TF motif (Figure 4F) and only occurred in neurons in the depolarized state (Figure S4D). In unstimulated neurons, KO caused gains of accessibility at AP-1 TF-binding elements (Figure S4D), consistent with previous studies.⁴ Analysis of the variance in accessibility across all TF motifs⁵³ showed that KO caused the greatest losses in accessibility after neuronal depolarization at the Rfx1/X-box motif (Figure S4E). Our results indicate that neuronal activity requires Arid2-containing PBAF to open chromatin at RFX/X-box sites.

We also compared the relative ability of KO and NT neurons to open chromatin in response to neuronal activity at the DNA elements (2,710) identified as requiring BAF ATPase activity to gain accessibility (Figure S4F). The analysis indicated that Arid2 KO reduces activity-dependent opening by BAF complexes by ~25% ($p < 0.001$) (Figure S4F). The modest contribution to BAF-dependent opening is consistent with the observation that the pan-complex subunits Brg1 and Smarcc2 are positioned at activity-responsive elements prior to neuronal activity (Figure 3E), which could indicate the presence of other classes of BAF complexes. Hence, PBAF partially contributes to the total response of BAF to neuronal activity.

While we cannot rule out that RFX TFs may interact with BAF complexes to recruit its activity, neither our proteomics nor transcriptomic datasets nor publicly available proteomic datasets show evidence supporting a direct interaction. Of the eight mammalian RFX TFs (RFX1-8), only three (Rfx3, Rfx1, and Rfx5) were detected in our total neuronal nuclear extracts by mass spectrometry (Figure S4G). Zero peptides of any of these were detected in our BAF IP-MS (Figure S4G). Only *Rfx3* and *Rfx7* were expressed at high levels in cortical neurons by RNA-seq (Figure S4H); however, neither those nor any of the other RFX TFs have been detected to interact with any of the 29 different BAF subunits in 2 different public compilations of protein interactomes (STRING^{54,55} and BioGRID^{54,55}) in either mouse or human cells.

Altogether, our analyses suggest that PBAF complexes containing Arid2 bind directly to DNA with sequence specificity. Since neuronal activity stabilizes the Arid2-Brg1 interaction (Figure 2C), and Brg1 is already bound to activity- and BAF-dependent elements before neuronal activity (Figure 3E), our ATAC-seq analyses indicate that assembly of PBAF (Figure 2) is important for sequence-specific function but not necessarily recruitment. Thus, neuronal activity triggers assembly (Figures 1 and 2) that corresponds to functional chromatin remodeling (Figures 3 and 4). The causal connection between assembly and recruitment on chromatin remains to be explored.

Neuronal activity causes immediate BAF phosphorylation

Neuronal activity triggers activation of poised TFs such as cyclic adenosine monophosphate (cAMP)-responsive element binding (CREB) and serum response factor (SRF) by phosphorylation⁵⁶ to drive activity-dependent transcription.^{13,30,33,35,36,39} We hypothesized that neuronal activity may similarly lead to phosphorylation of BAF subunits, and that activity-induced phosphoryla-

tion would regulate BAF assembly and chromatin remodeling activity.

Phosphoproteomic profiling of immunoprecipitated BAF complexes or total nuclear extracts from resting and depolarized cortical neurons revealed 38 different high-confidence phosphosites on 12 unique BAF subunits (Figure 5A; Table S1). This represents 41% of the 29 different proteins known to assemble into BAF complexes.¹⁸ Approximately half of these residues were also identified as phosphorylated in nine other mouse tissues or in mouse fibroblasts (Figure 5A). A specific set of ~6 residues on Smarcc2, Bcl7a, Smarca4, Dpf1, and Arid1a was significantly (p value ≤ 0.05 , fold change ≥ 1.5) hyper-phosphorylated after 10 and 30 min of depolarization, independent of changes in protein level (Figure 5B). The timescale of modification is comparable with the timescales of phosphorylation of other activity-regulated TFs and suggests that these six residues are direct targets of neuronal activity. Consistent with a recent report that identified phosphorylation of serine 1382 on Brg1 as required for proper stress response in mice,⁵⁷ we detected activity-induced hyper-phosphorylation of serine 1349 on Brg1 (equivalent to serine 1382 in other Brg1 isoforms) 10 min after depolarization. On two subunits (Brg1 and Dpf2), activity-dependent hyperphosphorylation at certain residues was concurrent with activity-dependent hypo-phosphorylation on other residues (Figure 5A). Blockade of calcium-responsive kinase and phosphatase activity selectively reversed activity-induced hyper- or hypo-phosphorylation in a residue-specific manner, with residues on the same BAF subunit responding differently to different kinases, suggesting a notable specificity of action (Figure 5A).

Phosphorylation does not affect BAF assembly

To identify the biochemical consequences of phosphorylation, we focused on Smarcc2, a core subunit common to both BAF and PBAF complexes and essential for the first steps of complex formation.¹⁸ Smarcc2 was hyper-phosphorylated by neuronal activity not only in Brg1-immunoprecipitates but also in total neuronal nuclear extracts (Figure 5A), suggesting it is a high-abundance event. Specifically, serine 586 on Smarcc2 was significantly hyper-phosphorylated after depolarization for 10 and 30 min in both datasets and attenuated after the addition of CaMKK, MEK, or DCLK inhibitors but not NFAT/CaN inhibitors (Figures 5A, 5B, S5A, and S5B), indicating dynamic regulation by calcium-induced signaling pathways. Other phosphosites on Smarcc2 are required for the differentiation of neurons and neural progenitors from ESCs.^{59,60} SMARCC2, the homologous human gene, is a high-confidence autism gene⁶¹ in which deleterious *de novo* variants have been found in individuals with neurodevelopmental delay.⁶² Reasoning that Smarcc2 regulation plays a rate-limiting role in neural development and represents a critical model of BAF function downstream of neuronal activity, we investigated how its activity-induced phosphorylation might affect BAF assembly and regulation of gene expression.

We generated FLAG-tagged Smarcc2 constructs with mutations at the serine 586 position to alanine (S586A), which cannot be phosphorylated, or to glutamate (S586E), which is chemically similar to a phospho-serine residue and mimics a constitutively phosphorylated Smarcc2 (Figure 5C). Co-expression of mutant or wild-type (WT) Smarcc2 constructs with green fluorescent

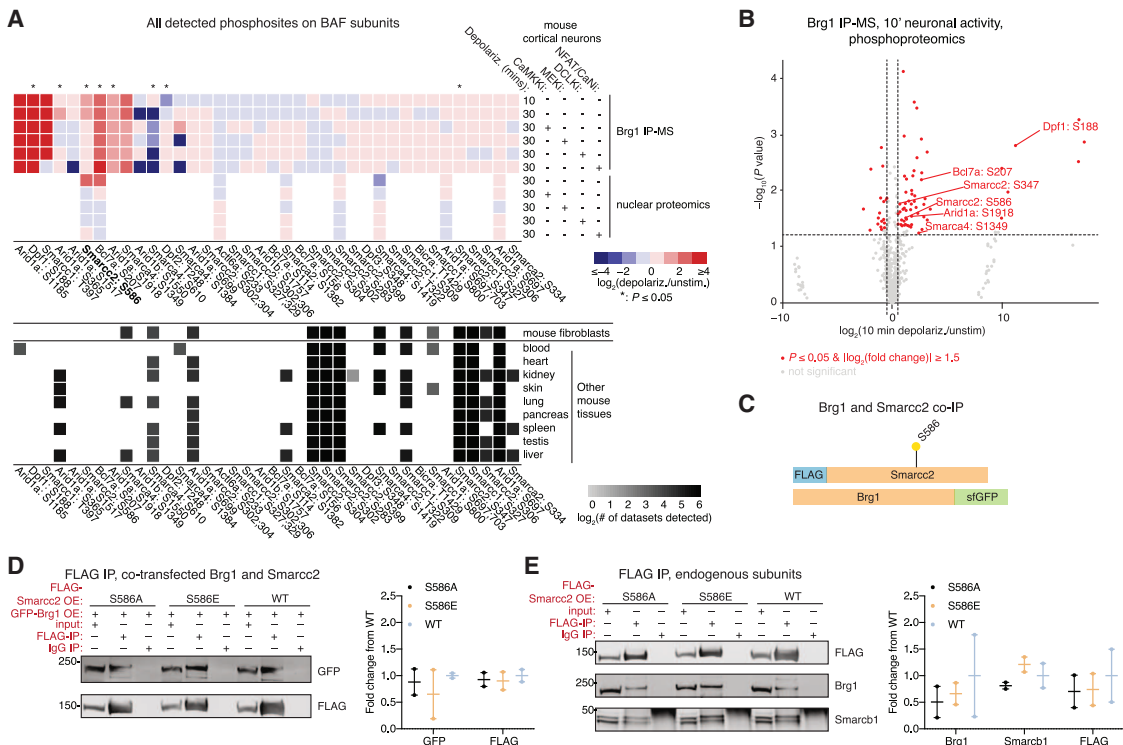


Figure 5. Neuronal activity causes immediate BAF phosphorylation

(A) Detected phosphosites on BAF subunits enriched after Brg1 IP-MS or detected in whole nuclear proteomics in neurons with or without depolarization to model neuronal activity and/or inhibitors of calcium-activated signaling, compared with phosphosites detected in public datasets of mouse tissue⁵⁸; 2–3 biological replicates per condition; *p* values computed by two-sided Wald test.

(B) Differential phosphosites ($p \leq 0.05$ and \log_2 fold change ≥ 1.5 or ≤ -1.5) on subunits enriched after Brg1 IP (norm. total protein) after 10 min of neuronal activity; two biological replicates. For (A) and (B): p values computed by two-sided unpaired t test.

(C) Schematic of constructs transfected in HEK293T cells; sfGFP: super-folder green fluorescent protein.

(D) FLAG IP after co-transfection of Brg1-sfGFP and FLAG-Smarcc2 and immunoblot for GFP.

(E) FLAG IP after transfection of FLAG-Smarc2 and immunoblot for endogenous Brg1 and Smarcb1 subunits. For (D) and (E): blots representative of two biological replicates; mean \pm SEM, p values computed by one-way ANOVAs between WT and mutants; no significant ($p < 0.05$) changes were detected. OE, over-expression.

See also Figure S5 and Data S1.

protein (GFP)-tagged Brg1 in HEK293T cells followed by FLAG IP showed that (1) S586 phosphorylation is not required for interaction with Brg1 (Figure 5D, comparison of WT to S586A), and (2) S586 phosphorylation is not sufficient to change the Smarcc2:Brg1 interaction (Figure 5D, comparison of WT to S586E). Both mutants incorporated comparably well to WT into endogenous BAF and PBAF complexes, as assessed by immunoblotting for endogenous subunits (Figure 5E). Neither mutation affected the protein stability of Smarcc2 in cells.

To assess the biochemical consequences of Smarcc2 phosphorylation in neurons, we generated Smarcc2 KO cortical neurons in culture and replaced the KO with an empty vector (Vec), WT, S586A, or S586E Smarcc2 constructs by overexpression (Figures S5C and S5D). KO was ~80% complete after 18 days of culture (DIV18), and mutants were well expressed at levels comparable to WT levels (comparison to co-infection of non-targeting guide RNA, NT, and empty vector, Vec, constructs [NT+Vec]) (Figure S5E). Co-immunoprecipitation of FLAG-Smarcc2 constructs and BAF and PBAF subunits

showed that neither Smarcc2 mutant affected incorporation into endogenous neuronal complexes (Figures S5F and S5G). Our data in neurons are consistent with our co-immunoprecipitation analyses in HEK293T cells and indicate that Smarcc2 phosphorylation does not affect complex assembly.

Smarcc2 phosphorylation is dispensable for the activity-dependent neuronal response

To assess the direct contribution of Smarcc2 hyper-phosphorylation to activity-dependent gene regulation, we analyzed the transcriptome and chromatin accessibility landscape of neurons in depolarized or unstimulated states after replacing endogenous Smarcc2 with Vec, mutant, or WT constructs as before (Figures 6A, S5D, and S5E). In response to depolarization, neurons with Smarcc2 deleted without replacement (KO+Vec) activated neuronal activity-induced genes including *Fos*, *Arc*, and *Npas4* as well as their unaltered counterparts (NT+Vec) did, but they aberrantly activated and repressed hundreds of other genes (adj. $p < 0.05$; 295 up and 491 down) that

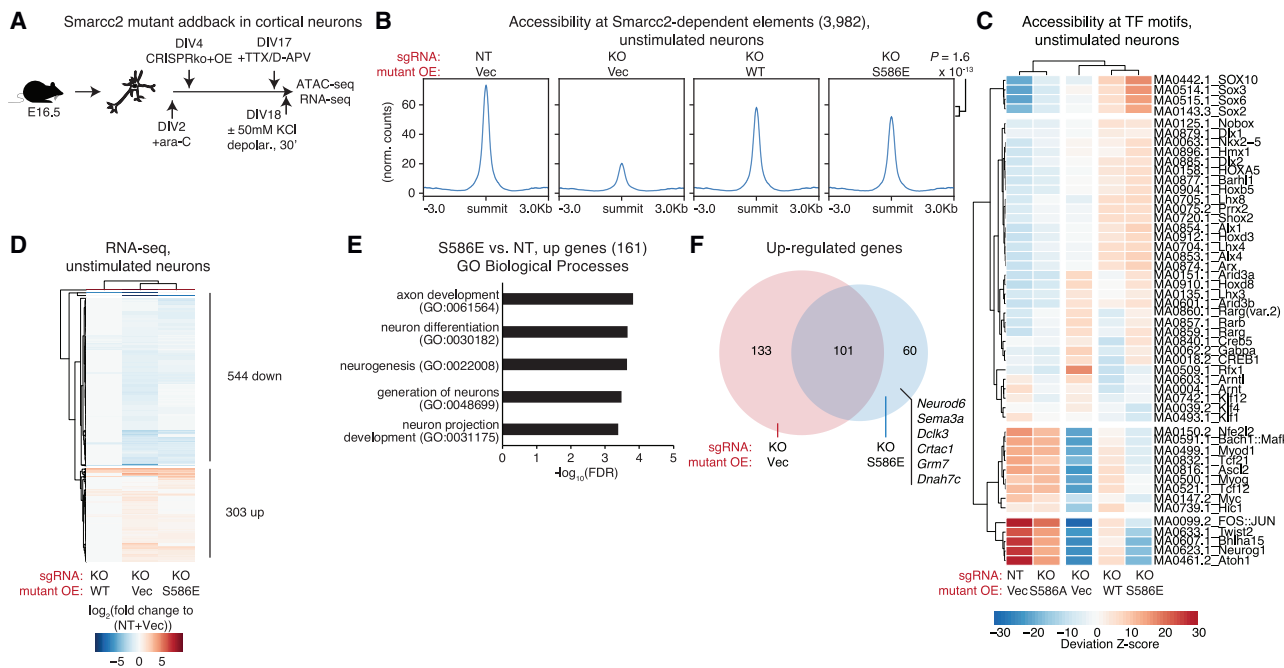


Figure 6. Smarcc2 phosphorylation redirects BAF activity

(A) Schematic of KO and replacement experiment to study Smarcc2 phosphorylation in neurons with or without depolarization to model neuronal activity, followed by ATAC-seq or RNA-seq. DIV, day *in vitro*.

(B) Chromatin accessibility at elements significantly decreased after Smarcc2 KO (adj. $p \leq 0.05$ and \log_2 fold change ≤ -0.5) in unstimulated neurons; two biological replicates; p value of difference in average accessibility computed by Kruskal-Wallis test.

(C) Accessibility at top 50 most variable transcription factor motifs across Smarcc2 alleles in unstimulated neurons.

(D) Differential gene expression (adj. $p \leq 0.05$ and \log_2 fold change ≥ 0.5 or ≤ -0.5) in unstimulated neurons across Smarcc2 alleles; 2–3 biological replicates. For (B) and (D): differential p values computed by two-sided Wald test and adjusted by Benjamini-Hochberg.

(E) GO biological processes enriched in genes induced by Smarcc2(S586E); p values computed by Fisher's exact test and adjusted by Benjamini-Hochberg.

(F) Overlap of upregulated genes (from D) between Smarcc2(KO) and Smarcc2(S586E). For (B)–(F): NT, non-targeting sgRNA; Vec, empty overexpression vector; KO, Smarcc2-targeting sgRNAs; WT, Smarcc2(WT); S586A, Smarcc2(S586A); or S586E, Smarcc2(S586E) overexpression.

See also Figures S6 and S7.

ordinarily remain unchanged (Figure S6A). Hierarchical clustering of depolarization-induced changes indicated that overexpression of either the WT or the S586A construct reversed the dysregulation of activity-induced gene expression caused by Smarcc2 KO (Figure S6A). On chromatin, depolarized neurons with Smarcc2 KO showed acute losses of accessibility at FOS:JUN and bHLH TF-binding sites, as expected,¹² which were reversed upon addback of WT or mutant constructs (Figure S6B).

Moreover, we analyzed activity-dependent dendritic outgrowth, a neurodevelopmental process on a longer timescale (18 h) that critically depends on BAF complexes.^{15,16,63} Smarcc2 deletion diminished activity-dependent growth after depolarization, but overexpression of either the WT or the S586A construct rescued the defect (Figure S6C). Our data indicate that phosphorylation of Smarcc2:S586 is dispensable for activity-dependent gene regulation and activity-dependent dendritic outgrowth.

Smarcc2 phosphorylation redirects BAF activity to Sox-binding sites

We reasoned that since neuronal activity led to hyper-phosphorylation of multiple Smarcc2 residues (Figures 5A and 5B), nearby

phosphosites may compensate for loss of any one phosphorylation. Therefore, we isolated the effects of Smarcc2:S586 phosphorylation by analyzing S586E phospho-mimic allele in resting neurons. Smarcc2 is required for maintenance of accessibility at 3,982 DNA elements in resting neurons including AP-1 and bHLH TF-binding sites (Figures 6B, 6C, and S7A) and regulates the expression of 684 genes (Figures 6D and S7C). Re-introduction of WT Smarcc2 restored accessibility at these loci (Figures 6B, 6C, and S7A) and reversed almost all changes in gene expression caused by Smarcc2 deletion (Figures 6D and S7C). In contrast, overexpression of the phospho-mimic, Smarcc2:S586E construct produced ~25% less restoration of accessibility at Smarcc2-regulated elements (Figures 6B and S7B) than the WT construct did and triggered aberrant expression of 438 other genes (Figures 6D and S7C). Replacement of Smarcc2 by the S586E mutant could not restore accessibility at AP-1 sites, which are known to require BAF,^{4,12} in contrast to replacement by the WT construct (Figure 6C). Overexpression of Smarcc2:S586E clustered more closely with Smarcc2 KO rather than Smarcc2 WT-overexpressed transcriptomes (Figures 6D and S7D).

Given that the Smarcc2 mutants did not show differences in protein stability or BAF complex incorporation (Figures 5E and

5F), we hypothesized that the S586E mutation may redirect BAF activity over the genome. Induced genes were enriched for biological processes related to nervous system development and neuronal projections (Figure 6E). Also, 37% of the S586E-induced genes were not inside the set of those affected by Smarcc2 deletion (Figure 6F), indicating some degree of gained function. These included genes implicated in axonal outgrowth and neuronal maturation, including *Sema3a*, *Neurod6*, and *Dnah7c* (Figure 6F). Moreover, the S586E mutant increased accessibility at Sox sites (Figure 6C). The gain of accessibility at Sox motifs was not observed in neurons with Smarcc2 deletion or replacement of Smarcc2 by the Smarcc2:S586A mutant construct (Figure 6C), indicating that it is a gain-of-function effect. Sox TFs direct different neural differentiation pathways.⁶⁴ Increased accessibility at Sox sites is consistent with enrichment of neurogenesis genes in S586E-induced transcripts (Figures 6E and 6F). Our data suggest that the S586E allele is multimorphic; it partially reduces chromatin accessibility at BAF-regulated regions, such as AP-1 sites, while also opening chromatin at Sox sites and activating neuronal maturation genes. Therefore, activity-induced hyper-phosphorylation of Smarcc2 may retarget BAF activity to produce accessibility for neurogenic TFs.

DISCUSSION

Most studies of BAF (mSWI/SNF) complexes in living cells have assumed its steady-state composition. Indeed, the subunits were originally defined by their ability to resist dissociation from the complexes under partially denaturing conditions.^{65–67} Here, we discovered that signals at the membrane trigger large-scale compositional changes in BAF complexes on a minute timescale. Acute neuronal activity led to assembly of BAF and PBAF as well as hyper- and hypo-phosphorylation of multiple subunits. Activity-induced assembly was also observed in MEFs. These biochemical changes were buffered upon inhibition of several different calcium-activated kinases and phosphatases. Our data indicate a biochemical decoding of membrane activity by controlling subunit composition of BAF in the nucleus.

Past studies have shown that the subunits maintain their association with the Brg1/Brm ATPase even in the presence of 3–5 M urea.^{65–67} Our results suggest the existence of an energy-dependent chaperone controlling assembly of the BAF complex in cells. While chaperones dedicated to this process have not been identified, Roberts and coworkers reported that the CUL4-DDB1 E3 ubiquitin ligase complex substrate receptor DCAF5 has a quality control function for BAF complexes and promotes the degradation of incompletely assembled complexes in the absence of SMARCB1 (BAF47).⁶⁸ Therefore, BAF-specific assembly chaperones may also exist. Because most subunits of BAF complexes are tumor suppressors, and 13 of the 29 subunits are genetically implicated in idiopathic intellectual disabilities or autism, the putative ATP-dependent chaperone is also likely a tumor suppressor with loss-of-function mutations in autism or intellectual disabilities.

Assembly and modification dynamics were responsible for directing chromatin remodeling activity. Focusing on neurons,

we mapped all activity-induced changes in accessible chromatin and determined that BAF activity is required for >1/10th of activity-dependent chromatin opening. Localization of remodeling in response to neuronal activity was in part directed by PBAF complexes, which were assembled concurrently. Hyper-phosphorylation of a core subunit, Smarcc2, also contributed modestly to localization of activity. In short, we provide evidence that the biochemical encoding of neuronal activity on BAF complexes directly impacts its nucleosome remodeling function on chromatin.

BAF complexes are generally considered to have little sequence specificity. However, we found that the RFX domain of Arid2 predicts locations of BAF activity over the genome after excitatory stimuli. This domain is mutated in human neurodevelopmental disorders such as idiopathic intellectual disability and Coffin-Siris syndrome (Figure 4). The RFX-binding site spans 14 nt and might provide an initial interaction with DNA and participate in stabilizing complexes on chromatin to facilitate nucleosome remodeling.

Neuronal activity remodels synapses and connections. The requirement of BAF ATPase function for opening chromatin at synaptic genes in response to neuronal activity (Figure 3) exemplifies the connection between the synapse and BAF. The kinetics of compositional and functional changes in BAF complexes parallel the kinetics of neuronal activity-induced gene expression,³² suggesting that the biochemical changes of neuronal activity observed here may facilitate activity-induced transcription directly. One such mechanism, the mediation of activity-induced RNA polymerase II elongation, was reported⁶⁹ while this manuscript was in review.

More than 1,400 different BAF complexes can be combinatorially assembled from 29 genes.¹⁸ In neural progenitors, subunit switching controls cell-cycle exit and differentiation.^{22,70–72} Could different environmental stimuli encode the assembly of unique BAF complexes to prompt different cell fates? In fibroblasts, BAF coordinates with cell-type-specific and broadly expressed TFs to establish accessibility at signal-dependent enhancers responsible for differentiation.¹² Different subunit compositions or modifications would form different composite surfaces that reprogram interactions with other TFs and retarget BAF on chromatin. The effects on chromatin of the multimorphic Smarcc2 allele that mimics hyper-phosphorylation exemplifies this (Figure 6).

Human genetic studies have indicated that BAF complexes play a surprisingly dominant role in neural development. *ARID1B* (BAF250B) is the most frequently mutated gene in human intellectual disability^{52,73} and is haploinsufficient for neural development. Other subunits show genetic variations associated with academic achievement and increased intelligence.^{6,7} These genetic studies indicate that the neural-specific nBAF complexes play a dosage-sensitive, rate-limiting role in development of the human brain. Recently *Arid1b* was found to execute its function on the social behavior in adult mice,⁷⁴ rather than, as previously expected, during development. Because the social defects caused by *Arid1b* deletion could be partially reversed by giving a selective 5-HT1b receptor agonist to adult animals,⁷⁴ it is possible that Arid1b and the nBAF complex execute their functions on a short timescale, perhaps by controlling membrane

channels or synaptic composition. Thus, the excitatory response of BAF could play a critical role not only in shaping the neural circuitry responsible for complex traits such as learning, memory, and social behavior but also in tuning these neural circuits in adult mammals, suggesting that the synapse-to-nucleus signaling response of BAF may be a therapeutic target.

Limitations of the study

This work models neuronal activity in mouse cultured cortical neurons and growth factor signaling in cultured fibroblasts, which are removed from their tissue environments containing other cell types and purified. Additionally, this study modeled activity using membrane depolarization by 50 mM KCl, an established protocol but with documented limitations.⁷⁵ KCl-mediated depolarization also activates many different intracellular signaling cascades. Future work could explore the findings on BAF regulation reported here in an animal using excitatory stimuli.

RESOURCE AVAILABILITY

Lead contact

Requests for further information and resources should be directed to the lead contact, Gerald R. Crabtree (crabtree@stanford.edu).

Materials availability

All materials and reagents will be available from authors upon request. This study did not generate new unique reagents.

Data and code availability

- Sequencing data have been deposited at GEO and are publicly available. Original blot scans are in [Figure S8](#). Microscopy data will be shared by the [lead contact](#) upon request. The mass spectrometry proteomics data have been deposited to the ProteomeXchange Consortium via the PRIDE⁷⁶ partner repository. All accession numbers are listed in the [key resources table](#).
- This paper does not report any original code.
- Any additional information required to reanalyze the data reported in this paper is available from the [lead contact](#) upon request.

ACKNOWLEDGMENTS

S.G. would like to thank L. Chen for advice in neuronal dissections and mouse husbandry, C. Weber for advice in organizing the proteomic analyses, N.S. Gray and F. Ferguson for providing the Dclk inhibitor, and E. Raz and A. Krogan for advice in performing the transcription factor motif analyses. All authors would like to thank members of the Crabtree lab for input and advice. The studies described were funded by a grant from HHMI to G.R.C. and NIH grants CA276167, CA163915, and MH126720-01 to G.R.C. Funding was provided to S.G. from NIH grant 5F31HD103339-03. Partial funding from NIH/NIGMS grants R01 GM67945 was provided to S.P.G. and R01 GM132129 to J.A.P.

AUTHOR CONTRIBUTIONS

S.G., W.W., and G.R.C. conceived the project. S.G. generated cultured neurons, performed cell biology, molecular biology, biochemical, neurobiological, and genomics experiments and computational analyses. S.A.N. generated cultured neurons and conducted biochemical and genomics experiments with S.G. W.W. assisted with neuronal dissections, biochemical experiments, and project design. J.A.P. and S.P.G. performed mass spectrometry (phospho)proteomics with extracts provided by S.G.; C.E. performed cloning under supervision of S.G. S.H.K. performed the Smarcc2 mutant ATAC-seq and the cortical neuronal RNA-seq together with S.G. H.Z.A. performed lentivirus pro-

duction under supervision of S.G. and G.R.C. K.C.R. analyzed activity-dependent dendritic outgrowth. S.G., S.A.N., and G.R.C. wrote the manuscript with input of all authors.

DECLARATION OF INTERESTS

G.R.C. is a founder and shareholder of Foghorn Therapeutics and Shenandoah Therapeutics.

STAR METHODS

Detailed methods are provided in the online version of this paper and include the following:

- KEY RESOURCES TABLE
- EXPERIMENTAL MODEL AND STUDY PARTICIPANT DETAILS
 - Animal Husbandry
 - Mouse Embryonic Fibroblast (MEF) cell culture
 - HEK293T Cell Culture
 - Primary Neuron Culture
- METHOD DETAILS
 - MEF Serum Stimulation
 - Membrane Depolarization by KCl Stimulation in Neurons
 - Other Pharmacological Treatments in Neurons
 - Lentivirus Production
 - CRISPR Constructs
 - Lentiviral Overexpression Constructs
 - Lentiviral Transduction of Neurons
 - Nuclear Extract Preparation
 - Immunoprecipitation (IP) from Neurons
 - Immunoprecipitation from HEK293T Cells
 - Glycerol Gradient
 - Sample Processing for Quantitative TMT-Proteomic Analysis
 - Mass Spectrometry Data Collection and Processing
 - Western Blotting
 - RNA Extraction, qPCR, and Sequencing Library Preparation
 - RNA-seq Analysis
 - ATAC-seq
 - ATAC-seq Analysis
 - CUT&RUN Experiment and Library Preparation
 - CUT&RUN Analysis
 - Activity-dependent Dendritic Outgrowth Experiment and Analysis
- QUANTIFICATION AND STATISTICAL ANALYSIS

SUPPLEMENTAL INFORMATION

Supplemental information can be found online at <https://doi.org/10.1016/j.molcel.2025.05.017>.

Received: October 24, 2023

Revised: April 2, 2025

Accepted: May 14, 2025

Published: June 9, 2025

REFERENCES

- Narlikar, G.J., Sundaramoorthy, R., and Owen-Hughes, T. (2013). Mechanisms and functions of ATP-dependent chromatin-remodeling enzymes. *Cell* 154, 490–503. <https://doi.org/10.1016/j.cell.2013.07.011>.
- Ronan, J.L., Wu, W., and Crabtree, G.R. (2013). From neural development to cognition: unexpected roles for chromatin. *Nat. Rev. Genet.* 14, 347–359. <https://doi.org/10.1038/nrg3413>.
- Son, E.Y., and Crabtree, G.R. (2014). The role of BAF (mSWI/SNF) complexes in mammalian neural development. *Am. J. Med. Genet. C Semin. Med. Genet.* 166C, 333–349. <https://doi.org/10.1002/ajmg.c.31416>.

4. Wenderski, W., Wang, L., Krokhotin, A., Walsh, J.J., Li, H., Shoji, H., Ghosh, S., George, R.D., Miller, E.L., Elias, L., et al. (2020). Loss of the neural-specific BAF subunit ACTL6B relieves repression of early response genes and causes recessive autism. *Proc. Natl. Acad. Sci. USA* 117, 10055–10066. <https://doi.org/10.1073/pnas.1908238117>.
5. Okbay, A., Beauchamp, J.P., Fontana, M.A., Lee, J.J., Pers, T.H., Rietveld, C.A., Turley, P., Chen, G.B., Emilsson, V., Meddens, S.F.W., et al. (2016). Genome-wide association study identifies 74 loci associated with educational attainment. *Nature* 533, 539–542. <https://doi.org/10.1038/nature17671>.
6. Savage, J.E., Jansen, P.R., Stringer, S., Watanabe, K., Bryois, J., de Leeuw, C.A., Nagel, M., Awasthi, S., Barr, P.B., Coleman, J.R.I., et al. (2018). Genome-wide association meta-analysis in 269,867 individuals identifies new genetic and functional links to intelligence. *Nat. Genet.* 50, 912–919. <https://doi.org/10.1038/s41588-018-0152-6>.
7. Sniekers, S., Stringer, S., Watanabe, K., Jansen, P.R., Coleman, J.R.I., Krapohl, E., Taskesen, E., Hammerschlag, A.R., Okbay, A., Zabaneh, D., et al. (2017). Genome-wide association meta-analysis of 78,308 individuals identifies new loci and genes influencing human intelligence. *Nat. Genet.* 49, 1107–1112. <https://doi.org/10.1038/ng.3869>.
8. Alberini, C.M., and Kandel, E.R. (2014). The regulation of transcription in memory consolidation. *Cold Spring Harb. Perspect. Biol.* 7, a021741. <https://doi.org/10.1101/cshperspect.a021741>.
9. Shaywitz, A.J., and Greenberg, M.E. (1999). CREB: a stimulus-induced transcription factor activated by a diverse array of extracellular signals. *Annu. Rev. Biochem.* 68, 821–861. <https://doi.org/10.1146/annurev.biochem.68.1.821>.
10. Flavell, S.W., Cowan, C.W., Kim, T.K., Greer, P.L., Lin, Y., Paradis, S., Griffith, E.C., Hu, L.S., Chen, C., and Greenberg, M.E. (2006). Activity-dependent regulation of MEF2 transcription factors suppresses excitatory synapse number. *Science* 311, 1008–1012. <https://doi.org/10.1126/science.1122511>.
11. Ebert, D.H., Gabel, H.W., Robinson, N.D., Kastan, N.R., Hu, L.S., Cohen, S., Navarro, A.J., Lyst, M.J., Ekiert, R., Bird, A.P., et al. (2013). Activity-dependent phosphorylation of MeCP2 threonine 308 regulates interaction with NCoR. *Nature* 499, 341–345. <https://doi.org/10.1038/nature12348>.
12. Vierbuchen, T., Ling, E., Cowley, C.J., Couch, C.H., Wang, X., Harmin, D.A., Roberts, C.W.M., and Greenberg, M.E. (2017). AP-1 Transcription Factors and the BAF Complex Mediate Signal-Dependent Enhancer Selection. *Mol. Cell* 68, 1067–1082. <https://doi.org/10.1016/j.molcel.2017.11.026>.
13. Yap, E.L., and Greenberg, M.E. (2018). Activity-Regulated Transcription: Bridging the Gap between Neural Activity and Behavior. *Neuron* 100, 330–348. <https://doi.org/10.1016/j.neuron.2018.10.013>.
14. Sharma, N., Pollina, E.A., Nagy, M.A., Yap, E.L., DiBiase, F.A., Hrvatin, S., Hu, L., Lin, C., and Greenberg, M.E. (2019). ARNT2 Tunes Activity-Dependent Gene Expression through NCoR2-Mediated Repression and NPAS4-Mediated Activation. *Neuron* 102, 390–406. <https://doi.org/10.1016/j.neuron.2019.02.007>.
15. Aizawa, H., Hu, S.C., Bobb, K., Balakrishnan, K., Ince, G., Gurevich, I., Cowan, M., and Ghosh, A. (2004). Dendrite development regulated by CREST, a calcium-regulated transcriptional activator. *Science* 303, 197–202. <https://doi.org/10.1126/science.1089845>.
16. Wu, J.I., Lessard, J., Olave, I.A., Qiu, Z., Ghosh, A., Graef, I.A., and Crabtree, G.R. (2007). Regulation of dendritic development by neuron-specific chromatin remodeling complexes. *Neuron* 56, 94–108. <https://doi.org/10.1016/j.neuron.2007.08.021>.
17. Hodges, C., Kirkland, J.G., and Crabtree, G.R. (2016). The Many Roles of BAF (mSWI/SNF) and PBAF Complexes in Cancer. *Cold Spring Harb. Perspect. Med.* 6, a026930. <https://doi.org/10.1101/cshperspect.a026930>.
18. Mashtalir, N., D'Avino, A.R., Michel, B.C., Luo, J., Pan, J., Otto, J.E., Zullo, H.J., McKenzie, Z.M., Kubiak, R.L., St Pierre, R., et al. (2018). Modular Organization and Assembly of SWI/SNF Family Chromatin Remodeling Complexes. *Cell* 175, 1272–1288. <https://doi.org/10.1016/j.cell.2018.09.032>.
19. Mashtalir, N., Dao, H.T., Sankar, A., Liu, H., Corin, A.J., Bagert, J.D., Ge, E.J., D'Avino, A.R., Filipovski, M., Michel, B.C., et al. (2021). Chromatin landscape signals differentially dictate the activities of mSWI/SNF family complexes. *Science* 373, 306–315. <https://doi.org/10.1126/science.abf8705>.
20. Hota, S.K., and Bruneau, B.G. (2016). ATP-dependent chromatin remodelling during mammalian development. *Development* 143, 2882–2897. <https://doi.org/10.1242/dev.128892>.
21. Yoo, A.S., Sun, A.X., Li, L., Shcheglovitov, A., Portmann, T., Li, Y., Lee-Messer, C., Dolmetsch, R.E., Tsien, R.W., and Crabtree, G.R. (2011). MicroRNA-mediated conversion of human fibroblasts to neurons. *Nature* 476, 228–231. <https://doi.org/10.1038/nature10323>.
22. Yoo, A.S., Staahl, B.T., Chen, L., and Crabtree, G.R. (2009). MicroRNA-mediated switching of chromatin-remodelling complexes in neural development. *Nature* 460, 642–646. <https://doi.org/10.1038/nature08139>.
23. Kim, T.K., Hemberg, M., Gray, J.M., Costa, A.M., Bear, D.M., Wu, J., Harmin, D.A., Laptev, M., Barbara-Haley, K., Kuersten, S., et al. (2010). Widespread transcription at neuronal activity-regulated enhancers. *Nature* 465, 182–187. <https://doi.org/10.1038/nature09033>.
24. Greer, P.L., and Greenberg, M.E. (2008). From synapse to nucleus: calcium-dependent gene transcription in the control of synapse development and function. *Neuron* 59, 846–860. <https://doi.org/10.1016/j.neuron.2008.09.002>.
25. Nettles, S.A., Ikeuchi, Y., Lefton, K.B., Abbasi, L., Erickson, A., Agwu, C., Papouin, T., Bonni, A., and Gabel, H.W. (2023). MeCP2 represses the activity of topoisomerase IIbeta in long neuronal genes. *Cell Rep.* 42, 113538. <https://doi.org/10.1016/j.celrep.2023.113538>.
26. Pollina, E.A., Gilliam, D.T., Landau, A.T., Lin, C., Pajarillo, N., Davis, C.P., Harmin, D.A., Yap, E.L., Vogel, I.R., Griffith, E.C., et al. (2023). A NPAS4-NuA4 complex couples synaptic activity to DNA repair. *Nature* 614, 732–741. <https://doi.org/10.1038/s41586-023-05711-7>.
27. Porter, E.G., and Dykhuizen, E.C. (2017). Individual Bromodomains of Polybromo-1 Contribute to Chromatin Association and Tumor Suppression in Clear Cell Renal Carcinoma. *J. Biol. Chem.* 292, 2601–2610. <https://doi.org/10.1074/jbc.M116.746875>.
28. Greenberg, M.E., and Ziff, E.B. (1984). Stimulation of 3T3 cells induces transcription of the c-fos proto-oncogene. *Nature* 311, 433–438. <https://doi.org/10.1038/311433a0>.
29. Park, J., and Kirkland, J.G. (2025). The role of the polybromo-associated BAF complex in development. *Biochem. Cell Biol.* 103, 1–8. <https://doi.org/10.1139/bcb-2024-0224>.
30. Graef, I.A., Wang, F., Charron, F., Chen, L., Neilson, J., Tessier-Lavigne, M., and Crabtree, G.R. (2003). Neurotrophins and netrins require calcineurin/NFAT signaling to stimulate outgrowth of embryonic axons. *Cell* 113, 657–670. [https://doi.org/10.1016/s0092-8674\(03\)00390-8](https://doi.org/10.1016/s0092-8674(03)00390-8).
31. Schmitt, J.M., Guire, E.S., Saneyoshi, T., and Soderling, T.R. (2005). Calmodulin-Dependent Kinase Kinase/Calmmodulin Kinase I Activity Gates Extracellular-Regulated Kinase-Dependent Long-Term Potentiation. *J. Neurosci.* 25, 1281–1290. <https://doi.org/10.1523/JNEUROSCI.4086-04.2005>.
32. Tyssowski, K.M., DeStefino, N.R., Cho, J.H., Dunn, C.J., Poston, R.G., Cart, C.E., Jones, R.D., Chang, S.M., Romeo, P., Wurzelmann, M.K., et al. (2018). Different Neuronal Activity Patterns Induce Different Gene Expression Programs. *Neuron* 98, 530–546. <https://doi.org/10.1016/j.neuron.2018.04.001>.
33. Bito, H., Deisseroth, K., and Tsien, R.W. (1996). CREB phosphorylation and dephosphorylation: a Ca(2+)- and stimulus duration-dependent switch for hippocampal gene expression. *Cell* 87, 1203–1214. [https://doi.org/10.1016/s0092-8674\(00\)81816-4](https://doi.org/10.1016/s0092-8674(00)81816-4).

34. Chatila, T., Anderson, K.A., Ho, N., and Means, A.R. (1996). A unique phosphorylation-dependent mechanism for the activation of Ca²⁺/calmodulin-dependent protein kinase type IV/GR. *J. Biol. Chem.* 271, 21542–21548. <https://doi.org/10.1074/jbc.271.35.21542>.
35. Deisseroth, K., Heist, E.K., and Tsien, R.W. (1998). Translocation of calmodulin to the nucleus supports CREB phosphorylation in hippocampal neurons. *Nature* 392, 198–202. <https://doi.org/10.1038/32448>.
36. Ma, H., Groth, R.D., Cohen, S.M., Emery, J.F., Li, B., Hoedt, E., Zhang, G., Neubert, T.A., and Tsien, R.W. (2014). γ CaMKII shuttles Ca(2)(+)/CaM to the nucleus to trigger CREB phosphorylation and gene expression. *Cell* 159, 281–294. <https://doi.org/10.1016/j.cell.2014.09.019>.
37. Shang, L., Kwon, Y.G., Nandy, S., Lawrence, D.S., and Edelman, A.M. (2003). Catalytic and regulatory domains of doublecortin kinase-1. *Biochemistry* 42, 2185–2194. <https://doi.org/10.1021/bi026913i>.
38. Shin, E., Kashiwagi, Y., Kuriu, T., Iwasaki, H., Tanaka, T., Koizumi, H., Gleeson, J.G., and Okabe, S. (2013). Doublecortin-like kinase enhances dendritic remodelling and negatively regulates synapse maturation. *Nat. Commun.* 4, 1440. <https://doi.org/10.1038/ncomms2443>.
39. Graef, I.A., Mermelstein, P.G., Stankunas, K., Neilson, J.R., Deisseroth, K., Tsien, R.W., and Crabtree, G.R. (1999). L-type calcium channels and GSK-3 regulate the activity of NF-ATc4 in hippocampal neurons. *Nature* 401, 703–708. <https://doi.org/10.1038/44378>.
40. Gorkin, D.U., Barozzi, I., Zhao, Y., Zhang, Y., Huang, H., Lee, A.Y., Li, B., Chiou, J., Wildberg, A., Ding, B., et al. (2020). An atlas of dynamic chromatin landscapes in mouse fetal development. *Nature* 583, 744–751. <https://doi.org/10.1038/s41586-020-2093-3>.
41. Iurlaro, M., Stadler, M.B., Masoni, F., Jagani, Z., Galli, G.G., and Schübeler, D. (2021). Mammalian SWI/SNF continuously restores local accessibility to chromatin. *Nat. Genet.* 53, 279–287. <https://doi.org/10.1038/s41588-020-00768-w>.
42. Schick, S., Grosche, S., Kohl, K.E., Drpic, D., Jaeger, M.G., Marella, N.C., Imrichova, H., Lin, J.G., Hofstätter, G., Schuster, M., et al. (2021). Acute BAF perturbation causes immediate changes in chromatin accessibility. *Nat. Genet.* 53, 269–278. <https://doi.org/10.1038/s41588-021-00777-3>.
43. Ernst, J., and Kellis, M. (2012). ChromHMM: automating chromatin-state discovery and characterization. *Nat. Methods* 9, 215–216. <https://doi.org/10.1038/nmeth.1906>.
44. Voigt, P., Tee, W.W., and Reinberg, D. (2013). A double take on bivalent promoters. *Genes Dev.* 27, 1318–1338. <https://doi.org/10.1101/gad.219626.113>.
45. McLean, C.Y., Bristor, D., Hiller, M., Clarke, S.L., Schaar, B.T., Lowe, C. B., Wenger, A.M., and Bejerano, G. (2010). GREAT improves functional interpretation of cis-regulatory regions. *Nat. Biotechnol.* 28, 495–501. <https://doi.org/10.1038/nbt.1630>.
46. Gajiwala, K.S., Chen, H., Cornille, F., Roques, B.P., Reith, W., Mach, B., and Burley, S.K. (2000). Structure of the winged-helix protein hRFX1 reveals a new mode of DNA binding. *Nature* 403, 916–921. <https://doi.org/10.1038/35002634>.
47. Sugiaman-Trapman, D., Vitezic, M., Jouhilahti, E.-M., Mathelier, A., Lauter, G., Misra, S., Daub, C.O., Kere, J., and Swoboda, P. (2018). Characterization of the human RFX transcription factor family by regulatory and target gene analysis. *BMC Genomics* 19, 181. <https://doi.org/10.1186/s12864-018-4564-6>.
48. Vierstra, J., Lazar, J., Sandstrom, R., Halow, J., Lee, K., Bates, D., Diegel, M., Dunn, D., Neri, F., Haugen, E., et al. (2020). Global reference mapping of human transcription factor footprints. *Nature* 583, 729–736. <https://doi.org/10.1038/s41586-020-2528-x>.
49. Bentsen, M., Goymann, P., Schultheis, H., Klee, K., Petrova, A., Wiegandt, R., Fust, A., Preussner, J., Kuenne, C., Braun, T., et al. (2020). ATAC-seq footprinting unravels kinetics of transcription factor binding during zygotic genome activation. *Nat. Commun.* 11, 4267. <https://doi.org/10.1038/s41467-020-18035-1>.
50. Wagner, F.R., Dienemann, C., Wang, H., Stützer, A., Tegunov, D., Urlaub, H., and Cramer, P. (2020). Structure of SWI/SNF chromatin remodeler RSC bound to a nucleosome. *Nature* 579, 448–451. <https://doi.org/10.1038/s41586-020-2088-0>.
51. Brahma, S., and Henikoff, S. (2019). RSC-Associated Subnucleosomes Define MNase-Sensitive Promoters in Yeast. *Mol. Cell* 73, 238–249. <https://doi.org/10.1016/j.molcel.2018.10.046>.
52. Gourisankar, S., Krokhotin, A., Wenderski, W., and Crabtree, G.R. (2024). Context-specific functions of chromatin remodelers in development and disease. *Nat. Rev. Genet.* 25, 340–361. <https://doi.org/10.1038/s41576-023-00666-x>.
53. Schep, A.N., Wu, B., Buenrostro, J.D., and Greenleaf, W.J. (2017). chromVAR: inferring transcription-factor-associated accessibility from single-cell epigenomic data. *Nat. Methods* 14, 975–978. <https://doi.org/10.1038/nmeth.4401>.
54. Szklarczyk, D., Kirsch, R., Koutrouli, M., Nastou, K., Mehryary, F., Hachilif, R., Gable, A.L., Fang, T., Doncheva, N.T., Pyysalo, S., et al. (2023). The STRING database in 2023: protein-protein association networks and functional enrichment analyses for any sequenced genome of interest. *Nucleic Acids Res.* 51, D638–D646. <https://doi.org/10.1093/nar/gkac1000>.
55. Oughtred, R., Rust, J., Chang, C., Breitkreutz, B.J., Stark, C., Willems, A., Boucher, L., Leung, G., Kolas, N., Zhang, F., et al. (2021). The BioGRID database: A comprehensive biomedical resource of curated protein, genetic, and chemical interactions. *Protein Sci.* 30, 187–200. <https://doi.org/10.1002/pro.3978>.
56. Flavell, S.W., and Greenberg, M.E. (2008). Signaling mechanisms linking neuronal activity to gene expression and plasticity of the nervous system. *Annu. Rev. Neurosci.* 31, 563–590. <https://doi.org/10.1146/annurev.neuro.31.060407.125631>.
57. Kim, B., Luo, Y., Zhan, X., Zhang, Z., Shi, X., Yi, J., Xuan, Z., and Wu, J. (2021). Neuronal activity-induced BRG1 phosphorylation regulates enhancer activation. *Cell Rep.* 36, 109357. <https://doi.org/10.1016/j.celrep.2021.109357>.
58. Hornbeck, P.V., Zhang, B., Murray, B., Kornhauser, J.M., Latham, V., and Skrzypek, E. (2015). PhosphoSitePlus, 2014: mutations, PTMs and recalibrations. *Nucleic Acids Res.* 43, D512–D520. <https://doi.org/10.1093/nar/gku1267>.
59. Ho, L., Ronan, J.L., Wu, J., Staahl, B.T., Chen, L., Kuo, A., Lessard, J., Nesvizhskii, A.I., Ranish, J., and Crabtree, G.R. (2009). An embryonic stem cell chromatin remodeling complex, esBAF, is essential for embryonic stem cell self-renewal and pluripotency. *Proc. Natl. Acad. Sci. USA* 106, 5181–5186. <https://doi.org/10.1073/pnas.0812889106>.
60. Ochoa, D., Jarnuzczak, A.F., Viéitez, C., Gehre, M., Soucheray, M., Mateus, A., Kleefeldt, A.A., Hill, A., Garcia-Alonso, L., Stein, F., et al. (2020). The functional landscape of the human phosphoproteome. *Nat. Biotechnol.* 38, 365–373. <https://doi.org/10.1038/s41587-019-0344-3>.
61. Satterstrom, F.K., Kosmicki, J.A., Wang, J., Breen, M.S., De Rubeis, S., An, J.Y., Peng, M., Collins, R., Grove, J., Klei, L., et al. (2020). Large-Scale Exome Sequencing Study Implicates Both Developmental and Functional Changes in the Neurobiology of Autism. *Cell* 180, 568–584. <https://doi.org/10.1016/j.cell.2019.12.036>.
62. Machol, K., Rousseau, J., Ehresmann, S., Garcia, T., Nguyen, T.T.M., Spillmann, R.C., Sullivan, J.A., Shashi, V., Jiang, Y.H., Stong, N., et al. (2019). Expanding the Spectrum of BAF-Related Disorders: De Novo Variants in SMARCC2 Cause a Syndrome with Intellectual Disability and Developmental Delay. *Am. J. Hum. Genet.* 104, 164–178. <https://doi.org/10.1016/j.ajhg.2018.11.007>.
63. Qiu, Z., and Ghosh, A. (2008). A calcium-dependent switch in a CREST-BRG1 complex regulates activity-dependent gene expression. *Neuron* 60, 775–787. <https://doi.org/10.1016/j.neuron.2008.09.040>.
64. Stevanovic, M., Drakulic, D., Lazic, A., Ninkovic, D.S., Schwirtlich, M., and Mojsin, M. (2021). SOX Transcription Factors as Important Regulators of Neuronal and Glial Differentiation During Nervous System

- Development and Adult Neurogenesis. *Front. Mol. Neurosci.* 14, 654031. <https://doi.org/10.3389/fnmol.2021.654031>.
65. Kadoch, C., Hargreaves, D.C., Hodges, C., Elias, L., Ho, L., Ranish, J., and Crabtree, G.R. (2013). Proteomic and bioinformatic analysis of mammalian SWI/SNF complexes identifies extensive roles in human malignancy. *Nat. Genet.* 45, 592–601. <https://doi.org/10.1038/ng.2628>.
66. Khavari, P.A., Peterson, C.L., Tamkun, J.W., Mendel, D.B., and Crabtree, G.R. (1993). BRG1 contains a conserved domain of the SWI2/SNF2 family necessary for normal mitotic growth and transcription. *Nature* 366, 170–174. <https://doi.org/10.1038/366170a0>.
67. Wang, W., Xue, Y., Zhou, S., Kuo, A., Cairns, B.R., and Crabtree, G.R. (1996). Diversity and specialization of mammalian SWI/SNF complexes. *Genes Dev.* 10, 2117–2130. <https://doi.org/10.1101/gad.10.17.2117>.
68. Radko-Juettner, S., Yue, H., Myers, J.A., Carter, R.D., Robertson, A.N., Mittal, P., Zhu, Z., Hansen, B.S., Donovan, K.A., Hunkeler, M., et al. (2024). Targeting DCAF5 suppresses SMARCB1-mutant cancer by stabilizing SWI/SNF. *Nature* 628, 442–449. <https://doi.org/10.1038/s41586-024-07250-1>.
69. Cornejo, K.G., Venegas, A., Sono, M.H., Door, M., Gutierrez-Ruiz, B., Karabedian, L.B., Nandi, S.G., Hadisurya, M., Tao, W.A., Dykhuizen, E.C., et al. (2024). Activity-assembled nBAF complex mediates rapid immediate early gene transcription by regulating RNA polymerase II productive elongation. *Cell Rep.* 43, 114877. <https://doi.org/10.1016/j.celrep.2024.114877>.
70. Braun, S.M.G., Petrova, R., Tang, J., Krokhotin, A., Miller, E.L., Tang, Y., Panagiotakos, G., and Crabtree, G.R. (2021). BAF subunit switching regulates chromatin accessibility to control cell cycle exit in the developing mammalian cortex. *Genes Dev.* 35, 335–353. <https://doi.org/10.1101/gad.342345.120>.
71. Lessard, J., Wu, J.I., Ranish, J.A., Wan, M., Winslow, M.M., Staahl, B.T., Wu, H., Aebersold, R., Graef, I.A., and Crabtree, G.R. (2007). An essential switch in subunit composition of a chromatin remodeling complex during neural development. *Neuron* 55, 201–215. <https://doi.org/10.1016/j.neuron.2007.06.019>.
72. Wu, J.I., Lessard, J., and Crabtree, G.R. (2009). Understanding the words of chromatin regulation. *Cell* 136, 200–206. <https://doi.org/10.1016/j.cell.2009.01.009>.
73. Valencia, A.M., Sankar, A., Van Der Sluijs, P.J., Satterstrom, F.K., Fu, J., Talkowski, M.E., Vergano, S.A.S., Santen, G.W.E., and Kadoch, C. (2023). Landscape of mSWI/SNF chromatin remodeling complex perturbations in neurodevelopmental disorders. *Nat. Genet.* 55, 1400–1412. <https://doi.org/10.1038/s41588-023-01451-6>.
74. Walsh, J.J., Llorach, P., Cardozo Pinto, D.F., Wenderski, W., Christoffel, D.J., Salgado, J.S., Heifets, B.D., Crabtree, G.R., and Malenka, R.C. (2021). Systemic enhancement of serotonin signaling reverses social deficits in multiple mouse models for ASD. *Neuropsychopharmacology* 46, 2000–2010. <https://doi.org/10.1038/s41386-021-01091-6>.
75. Rienecker, K.D.A., Poston, R.G., and Saha, R.N. (2020). Merits and Limitations of Studying Neuronal Depolarization-Dependent Processes Using Elevated External Potassium. *ASN Neuro* 12, 1759091420974807. <https://doi.org/10.1177/1759091420974807>.
76. Perez-Riverol, Y., Bandla, C., Kundu, D.J., Kamatchinathan, S., Bai, J., Hewapathirana, S., John, N.S., Prakash, A., Walzer, M., Wang, S., et al. (2025). The PRIDE database at 20 years: 2025 update. *Nucleic Acids Res.* 53, D543–D553. <https://doi.org/10.1093/nar/gkae1011>.
77. Buenrostro, J.D., Wu, B., Chang, H.Y., and Greenleaf, W.J. (2015). ATAC-seq: A Method for Assaying Chromatin Accessibility Genome-Wide. *Curr. Protoc. Mol. Biol.* 109, 21.29.1–21.29.9. <https://doi.org/10.1002/0471142727.mb2129s109>.
78. Meers, M.P., Bryson, T.D., Henikoff, J.G., and Henikoff, S. (2019). Improved CUT&RUN chromatin profiling tools. *eLife* 8, e46314. <https://doi.org/10.7554/eLife.46314>.
79. Skene, P.J., Henikoff, J.G., and Henikoff, S. (2018). Targeted in situ genome-wide profiling with high efficiency for low cell numbers. *Nat. Protoc.* 13, 1006–1019. <https://doi.org/10.1038/nprot.2018.015>.
80. Ferguson, F.M., Nabet, B., Raghavan, S., Liu, Y., Leggett, A.L., Kuljanin, M., Kalekar, R.L., Yang, A., He, S., Wang, J., et al. (2020). Discovery of a selective inhibitor of doublecortin like kinase 1. *Nat. Chem. Biol.* 16, 635–643. <https://doi.org/10.1038/s41589-020-0506-0>.
81. Ramírez, F., Ryan, D.P., Grüning, B., Bhardwaj, V., Kilpert, F., Richter, A.S., Heyne, S., Dündar, F., and Manke, T. (2016). deepTools2: a next generation web server for deep-sequencing data analysis. *Nucleic Acids Res.* 44, W160–W165. <https://doi.org/10.1093/nar/gkw257>.
82. Love, M.I., Huber, W., and Anders, S. (2014). Moderated estimation of fold change and dispersion for RNA-seq data with DESeq2. *Genome Biol.* 15, 550. <https://doi.org/10.1186/s13059-014-0550-8>.
83. Bray, N.L., Pimentel, H., Melsted, P., and Pachter, L. (2016). Near-optimal probabilistic RNA-seq quantification. *Nat. Biotechnol.* 34, 525–527. <https://doi.org/10.1038/nbt.3519>.
84. Chen, E.Y., Tan, C.M., Kou, Y., Duan, Q., Wang, Z., Meirelles, G.V., Clark, N.R., and Ma'ayan, A. (2013). Enrichr: interactive and collaborative HTML5 gene list enrichment analysis tool. *BMC Bioinformatics* 14, 128. <https://doi.org/10.1186/1471-2105-14-128>.
85. Mi, H., Muruganujan, A., and Thomas, P.D. (2013). PANTHER in 2013: modeling the evolution of gene function, and other gene attributes, in the context of phylogenetic trees. *Nucleic Acids Res.* 41, D377–D386. <https://doi.org/10.1093/nar/gks1118>.
86. Thomas, P.D., Ebert, D., Muruganujan, A., Mushayahama, T., Albou, L.P., and Mi, H. (2022). PANTHER: Making genome-scale phylogenetics accessible to all. *Protein Sci.* 31, 8–22. <https://doi.org/10.1002/pro.4218>.
87. Martin, M. (2011). Cutadapt removes adapter sequences from high-throughput sequencing reads. *EMBnet.journal* 17, 10. <https://doi.org/10.14806/ej.17.1.200>.
88. Zhang, Y., Liu, T., Meyer, C.A., Eeckhoute, J., Johnson, D.S., Bernstein, B.E., Nusbaum, C., Myers, R.M., Brown, M., Li, W., et al. (2008). Model-based Analysis of ChIP-Seq (MACS). *Genome Biol.* 9, R137. <https://doi.org/10.1186/gb-2008-9-9-r137>.
89. Heinz, S., Benner, C., Spann, N., Bertolino, E., Lin, Y.C., Laslo, P., Cheng, J.X., Murre, C., Singh, H., and Glass, C.K. (2010). Simple combinations of lineage-determining transcription factors prime cis-regulatory elements required for macrophage and B cell identities. *Mol. Cell* 38, 576–589. <https://doi.org/10.1016/j.molcel.2010.05.004>.
90. Quinlan, A.R., and Hall, I.M. (2010). BEDTools: a flexible suite of utilities for comparing genomic features. *Bioinformatics* 26, 841–842. <https://doi.org/10.1093/bioinformatics/btq033>.
91. Li, H., Handsaker, B., Wysoker, A., Fennell, T., Ruan, J., Homer, N., Marth, G., Abecasis, G., and Durbin, R.; 1000 Genome Project Data Processing Subgroup (2009). The Sequence Alignment/Map format and SAMtools. *Bioinformatics* 25, 2078–2079. <https://doi.org/10.1093/bioinformatics/btp352>.
92. Arshadi, C., Günther, U., Eddison, M., Harrington, K.I.S., and Ferreira, T.A. (2021). SNT: a unifying toolbox for quantification of neuronal anatomy. *Nat. Methods* 18, 374–377. <https://doi.org/10.1038/s41592-021-01105-7>.
93. Chambers, M.C., Maclean, B., Burke, R., Amodei, D., Ruderman, D.L., Neumann, S., Gatto, L., Fischer, B., Pratt, B., Egertson, J., et al. (2012). A cross-platform toolkit for mass spectrometry and proteomics. *Nat. Biotechnol.* 30, 918–920. <https://doi.org/10.1038/nbt.2377>.
94. Hathaway, N.A., Bell, O., Hodges, C., Miller, E.L., Neel, D.S., and Crabtree, G.R. (2012). Dynamics and memory of heterochromatin in living cells. *Cell* 149, 1447–1460. <https://doi.org/10.1016/j.cell.2012.03.052>.
95. Maze, I., Wenderski, W., Noh, K.M., Bagot, R.C., Tzavaras, N., Purushothaman, I., Elsässer, S.J., Guo, Y., Ionete, C., Hurd, Y.L., et al. (2015). Critical Role of Histone Turnover in Neuronal Transcription and

- Plasticity. *Neuron* 87, 77–94. <https://doi.org/10.1016/j.neuron.2015.06.014>.
96. Ataman, B., Boulting, G.L., Harmin, D.A., Yang, M.G., Baker-Salisbury, M., Yap, E.L., Malik, A.N., Mei, K., Rubin, A.A., Spiegel, I., et al. (2016). Evolution of Osteocrin as an activity-regulated factor in the primate brain. *Nature* 539, 242–247. <https://doi.org/10.1038/nature20111>.
97. Bartel, D.P., Sheng, M., Lau, L.F., and Greenberg, M.E. (1989). Growth factors and membrane depolarization activate distinct programs of early response gene expression: dissociation of fos and jun induction. *Genes Dev.* 3, 304–313. <https://doi.org/10.1101/gad.3.3.304>.
98. Braun, S.M.G., Kirkland, J.G., Chory, E.J., Husmann, D., Calarco, J.P., and Crabtree, G.R. (2017). Rapid and reversible epigenome editing by endogenous chromatin regulators. *Nat. Commun.* 8, 560. <https://doi.org/10.1038/s41467-017-00644-y>.
99. Doench, J.G., Fusi, N., Sullender, M., Hegde, M., Vainberg, E.W., Donovan, K.F., Smith, I., Tothova, Z., Wilen, C., Orchard, R., et al. (2016). Optimized sgRNA design to maximize activity and minimize off-target effects of CRISPR-Cas9. *Nat. Biotechnol.* 34, 184–191. <https://doi.org/10.1038/nbt.3437>.
100. Wingfield, P. (2001). Protein precipitation using ammonium sulfate. *Curr. Protoc. Protein Sci.* Appendix 3, Appendix 3F. <https://doi.org/10.1002/0471140864.psa03fs13>.
101. Lorch, Y., Maier-Davis, B., and Kornberg, R.D. (2018). Histone Acetylation Inhibits RSC and Stabilizes the +1 Nucleosome. *Mol. Cell* 72, 594–600. <https://doi.org/10.1016/j.molcel.2018.09.030>.
102. Hirano, R., Ehara, H., Kujirai, T., Uejima, T., Takizawa, Y., Sekine, S.I., and Kurumizaka, H. (2022). Structural basis of RNA polymerase II transcription on the chromatosome containing linker histone H1. *Nat. Commun.* 13, 7287. <https://doi.org/10.1038/s41467-022-35003-z>.
103. Fulton, S.L., Wenderski, W., Lepack, A.E., Eagle, A.L., Fanutza, T., Bastle, R.M., Ramakrishnan, A., Hays, E.C., Neal, A., Bendl, J., et al. (2022). Rescue of deficits by Brwd1 copy number restoration in the Ts65Dn mouse model of Down syndrome. *Nat. Commun.* 13, 6384. <https://doi.org/10.1038/s41467-022-34200-o>.
104. Sandoval, G.J., Pulice, J.L., Pakula, H., Schenone, M., Takeda, D.Y., Pop, M., Boulay, G., Williamson, K.E., McBride, M.J., Pan, J., et al. (2018). Binding of TMPRSS2-ERG to BAF Chromatin Remodeling Complexes Mediates Prostate Oncogenesis. *Mol. Cell* 71, 554–566. <https://doi.org/10.1016/j.molcel.2018.06.040>.
105. Navarrete-Perea, J., Yu, Q., Gygi, S.P., and Paulo, J.A. (2018). Streamlined Tandem Mass Tag (SL-TMT) Protocol: An Efficient Strategy for Quantitative (Phospho)proteome Profiling Using Tandem Mass Tag-Synchronous Precursor Selection-MS3. *J. Proteome Res.* 17, 2226–2236. <https://doi.org/10.1021/acs.jproteome.8b00217>.
106. Rappaport, J., Ishihama, Y., and Mann, M. (2003). Stop and go extraction tips for matrix-assisted laser desorption/ionization, nanoelectrospray, and LC/MS sample pretreatment in proteomics. *Anal. Chem.* 75, 663–670. <https://doi.org/10.1021/ac026117i>.
107. Paulo, J.A., O'Connell, J.D., Everley, R.A., O'Brien, J., Gygi, M.A., and Gygi, S.P. (2016). Quantitative mass spectrometry-based multiplexing compares the abundance of 5000 *S. cerevisiae* proteins across 10 carbon sources. *J. Proteomics* 148, 85–93. <https://doi.org/10.1016/j.jprot.2016.07.005>.
108. Saba, J., Bonneil, E., Pomiès, C., Eng, K., and Thibault, P. (2009). Enhanced sensitivity in proteomics experiments using FAIMS coupled with a hybrid linear ion trap/Orbitrap mass spectrometer. *J. Proteome Res.* 8, 3355–3366. <https://doi.org/10.1021/pr801106a>.
109. Beausoleil, S.A., Villén, J., Gerber, S.A., Rush, J., and Gygi, S.P. (2006). A probability-based approach for high-throughput protein phosphorylation analysis and site localization. *Nat. Biotechnol.* 24, 1285–1292. <https://doi.org/10.1038/nbt1240>.
110. Huttlin, E.L., Jedrychowski, M.P., Elias, J.E., Goswami, T., Rad, R., Beausoleil, S.A., Villén, J., Haas, W., Sowa, M.E., and Gygi, S.P. (2010). A tissue-specific atlas of mouse protein phosphorylation and expression. *Cell* 143, 1174–1189. <https://doi.org/10.1016/j.cell.2010.12.001>.
111. Elias, J.E., and Gygi, S.P. (2007). Target-decoy search strategy for increased confidence in large-scale protein identifications by mass spectrometry. *Nat. Methods* 4, 207–214. <https://doi.org/10.1038/nmeth1019>.
112. McAlister, G.C., Huttlin, E.L., Haas, W., Ting, L., Jedrychowski, M.P., Rogers, J.C., Kuhn, K., Pike, I., Grothe, R.A., Blelhow, J.D., et al. (2012). Increasing the multiplexing capacity of TMTs using reporter ion isotopologues with isobaric masses. *Anal. Chem.* 84, 7469–7478. <https://doi.org/10.1021/ac30152t>.
113. Nie, Z., Xue, Y., Yang, D., Zhou, S., Deroo, B.J., Archer, T.K., and Wang, W. (2000). A specificity and targeting subunit of a human SWI/SNF family-related chromatin-remodeling complex. *Mol. Cell. Biol.* 20, 8879–8888. <https://doi.org/10.1128/MCB.20.23.8879-8888.2000>.
114. Xue, Y., Canman, J.C., Lee, C.S., Nie, Z., Yang, D., Moreno, G.T., Young, M.K., Salmon, E.D., and Wang, W. (2000). The human SWI/SNF-B chromatin-remodeling complex is related to yeast rsc and localizes at kinetochore of mitotic chromosomes. *Proc. Natl. Acad. Sci. USA* 97, 13015–13020. <https://doi.org/10.1073/pnas.240208597>.
115. Zhu, A., Ibrahim, J.G., and Love, M.I. (2019). Heavy-tailed prior distributions for sequence count data: removing the noise and preserving large differences. *Bioinformatics* 35, 2084–2092. <https://doi.org/10.1093/bioinformatics/bty895>.
116. Kolde, R. (2018) Pheatmap: Pretty Heatmaps.
117. Maor-Nof, M., Shipony, Z., Marinov, G.K., Greenleaf, W.J., and Gitler, A.D. (2021). An optimized ATAC-seq protocol for genome-wide mapping of active regulatory elements in primary mouse cortical neurons. *Star Protoc.* 2, 100854. <https://doi.org/10.1016/j.xpro.2021.100854>.
118. Liu, N., Hargreaves, V.V., Zhu, Q., Kurland, J.V., Hong, J., Kim, W., Sher, F., Macias-Trevino, C., Rogers, J.M., Kurita, R., et al. (2018). Direct Promoter Repression by BCL11A Controls the Fetal to Adult Hemoglobin Switch. *Cell* 173, 430–442. <https://doi.org/10.1016/j.cell.2018.03.016>.
119. Amemiya, H.M., Kundaje, A., and Boyle, A.P. (2019). The ENCODE Blacklist: Identification of Problematic Regions of the Genome. *Sci. Rep.* 9, 9354. <https://doi.org/10.1038/s41598-019-45839-z>.
120. Perez, G., Barber, G.P., Benet-Pages, A., Casper, J., Clawson, H., Diekhans, M., Fischer, C., Gonzalez, J.N., Hinrichs, A.S., Lee, C.M., et al. (2025). The UCSC Genome Browser database: 2025 update. *Nucleic Acids Res.* 53, D1243–D1249. <https://doi.org/10.1093/nar/gkae974>.

STAR★METHODS

KEY RESOURCES TABLE

REAGENT or RESOURCE	SOURCE	IDENTIFIER
Antibodies		
Mouse anti-SMARCA4/Brg1 (H-10)	Santa Cruz Biotechnology	Cat# sc-374197; RRID: AB_10990135
Rabbit anti-Pbrm1/Baf180	The Crabtree Laboratory	N/A
Rabbit anti-Smarcc2/Baf170	The Crabtree Laboratory	N/A
Mouse anti-BAF170 (E-6)	Santa Cruz Biotechnology	Cat# sc-17838; RRID: AB_2286337
Mouse anti-Ini1/Baf47/SMARCB1 (A-5)	Santa Cruz Biotechnology	Cat# sc-166165; RRID: AB_2270651
Rabbit anti-PHF10/Baf45a	GeneTex	Cat# GTX116314; RRID: AB_11176023
Mouse anti-CREST (D-7)	Santa Cruz Biotechnology	Cat# sc-515827; RRID: N/A
Mouse anti-HDAC1 (10E2)	Santa Cruz Biotechnology	Cat# sc-81598; RRID: AB_2118083
Mouse anti-BRD7	Santa Cruz Biotechnology	Cat# sc-376180; RRID: AB_10989389
Mouse anti-ARID2 (E-3)	Santa Cruz Biotechnology	Cat# sc-166117; RRID: AB_2060382
Chicken anti-GFP	Aves Labs	Cat# GFP-1020; RRID: AB_10000240
Rabbit anti-cFos	Cell Signaling Technology	Cat# 2250; RRID: AB_2247211
Mouse anti-FLAG	Sigma-Aldrich	Cat# F1804; RRID: AB_262044
Rabbit anti-GFP	Thermo Fisher Scientific	Cat# A-6455; RRID: AB_221570
Mouse anti-Tubulin (TUJ1)	Covance	Cat# MMS-435P; RRID: AB_2313773
Mouse anti-GAPDH (6CS)	Santa Cruz Biotechnology	Cat# sc-32233; RRID: AB_627679
Rabbit β -Actin (13E5)	Cell Signaling Technology	Cat# 4970; RRID: AB_2223172
Rabbit anti-Histone H3	Abcam	Cat# ab1791; RRID: AB_302613
Rabbit anti-Vinculin	Thermo Fisher Scientific	Cat# 700062; RRID: AB_2532280
Mouse IgG	Santa Cruz Biotechnology	Cat# sc-2025; RRID: AB_737182
Rabbit IgG	Cell Signaling Technology	Cat# 2729; RRID: AB_1031062
IRDye 800CW Donkey anti-Rabbit IgG	LICORbio	Cat# 926-32213; RRID: AB_621848
IRDye 800CW Donkey anti-Mouse IgG	LICORbio	Cat# 926-32212; RRID: AB_621847
IRDye 800CW Goat anti-Rabbit IgG	LICORbio	Cat# 926-32211; RRID: AB_621843
IRDye 800CW Goat anti-Mouse IgG	LICORbio	Cat# 926-32210; RRID: AB_621842
IRDye 680RD Goat anti-Mouse IgG	LICORbio	Cat# 926-68070; RRID: AB_10956588
IRDye 680RD Goat anti-Rabbit IgG	LICORbio	Cat# 926-68071; RRID: AB_10956166
Normal Goat Serum	Jackson ImmunoResearch Laboratories	Cat# 005-000-121
Normal Donkey Serum	Jackson ImmunoResearch Laboratories	Cat# 017-000-121
Bacterial and virus strains		
One-Shot Stbl3 chemically competent <i>E. coli</i>	Invitrogen	Cat# C7373-03
Chemicals, peptides, and recombinant proteins		
Dynabeads Protein G	Thermo Fisher Scientific	Cat# 10009D
BS3 (bis(sulfosuccinimidyl)suberate)	Thermo Fisher Scientific	Cat# A39266
Benzonase Nuclease	Millipore-Sigma	Cat# E1014-25KU
Trichloroacetic acid solution	Millipore-Sigma	Cat# T0699
Polyethylenimine Max (PEI MAX) (MW 40,000)	Polysciences	Cat# 24765
TRIsure	Bioline	Cat# BIO-38033
Chymostatin	Millipore-Sigma	Cat# 230790
Leupeptin	Millipore-Sigma	Cat# 108975
Pepstatin A	Millipore-Sigma	Cat# 516481

(Continued on next page)

Continued

REAGENT or RESOURCE	SOURCE	IDENTIFIER
Protease Inhibitor	Millipore-Sigma	Cat# 4693132001
PhosSTOP phosphatase inhibitor	Millipore-Sigma	Cat# 4906845001
Deoxyribonuclease I	Worthington Biochemical Corporation	Cat# LS002058
Digitonin	Millipore-Sigma	Cat# 300410-250MG
Spermidine trihydrochloride	Millipore-Sigma	Cat# S2501-1G
Tn5 transposase	Buenrostro et al. ⁷⁷	N/A
Concanavalin A	EpiCypher	Cat# 21-1411
pA-MNase	Skene et al. ^{78,79}	N/A
CaMKKi inhibitor (CaMKKi)	Selleckchem	Cat# STO-609
Mirdametinib (PD0325901) (MEK1/2i)	Selleckchem	Cat# S1036
DCLK1/2 inhibitor (DCLK1i)	Ferguson et al. ⁸⁰	N/A
FHT1015	Foghorn Therapeutics	N/A
Cyclosporin A (CsA)	MedChem Express	Cat# HY-B0579
FK506 (Tacrolimus)	Abcam	Cat# ab120223
Tetrodotoxin citrate	Tocris Bioscience	Cat# 1069
D-AP5	Tocris Bioscience	Cat# 0106
Critical commercial assays		
Direct-zol RNA Miniprep Kits	Zymo Research	Cat# R2062
DNA Clean & Concentrator-5	Zymo Research	Cat# D4013
ZymoPURE II Plasmid Midiprep Kit	Zymo Research	Cat# D4200
Bio-Rad Protein Assay Dye (Bradford)	Bio-Rad	Cat# 500-0006
Lenti-X GoStix Plus	Takara	Cat# 631281
SensiFAST cDNA Synthesis Kit	Bioline	Cat# BIO-65054
SensiFAST SYBR Lo-ROX Kit	Bioline	Cat# BIO-94020
Q5 Site-Directed Mutagenesis Kit	New England Biolabs	Cat# E0554S
Neural Tissue Dissociation Kits	Miltenyi Biotech	Cat# 130-092-628
Mouse Neuron Nucleofector® Kit	Lonza	Cat# VPG-1001
High Sensitivity D1000 Reagents (Sample Buffer & Ladder)	Agilent Technologies	Cat# 5067-5585
High Sensitivity D1000 ScreenTapes	Agilent Technologies	Cat# 5067-5584
PhiX Control v3	Illumina	Cat# FC-110-3001
NEBNext rRNA Depletion Kit v2 (Human/Mouse/Rat)	New England Biolabs	Cat# E7400
NEBNext Poly(A) mRNA Magnetic Isolation Module	New England Biolabs	Cat# E7490S
NEBNext Ultra II DNA Library Prep with Sample Purification Beads	New England Biolabs	Cat# E7103S
NEBNext MultiplexOligos for Illumina (Dual Index Primers Set 1)	New England Biolabs	Cat# E7600S
NEBNext Ultra II Directional RNA Library Prep Kit	New England Biolabs	Cat# E7760S
Deposited data		
Deep sequencing datasets from this study	This paper	GEO: GSE245256
Mass spectrometry data from this study	This paper	PRIDE: PXD046031
Experimental models: Cell lines		
Primary cortical neurons	Derived from E16.5 cortex dissected from pure CD-1 mice obtained from Charles River	N/A
Mouse embryonic fibroblasts (MEFs)	The Crabtree Laboratory	N/A
HEK293T cells	Clontech	Cat# 632180

(Continued on next page)

Continued

REAGENT or RESOURCE	SOURCE	IDENTIFIER
Experimental models: Organisms/strains		
CD-1 mice, timed pregnant females	Charles River	Cat# Crl:CD1(ICR); RRID: IMSR_CRL:022
Oligonucleotides		
cFos FWD: CGGGTTCAACGCCGACTA	This paper	N/A
cFos REV: TTGGCACTAGAGACGGACAGA	This paper	N/A
Gapdh FWD: CTGACGTGCCGCTGGAGAAC	This paper	N/A
Gapdh REV: CCCGGCATCGAAGGTGGAAGAGT	This paper	N/A
Smarcc2 gRNA 1: GCGTCCATGCCATTGACCG	This paper	N/A
Smarcc2 gRNA 2: ACACCGACACATTCAACGAG	This paper	N/A
Smarcc2 gRNA 3: GACAGGATACACAACATGGG	This paper	N/A
Arid2 gRNA 1: ACTTGCAGTAAATTAGCTG	This paper	N/A
Arid2 gRNA 2: GAGGATAAGCTTCCCCCTG	This paper	N/A
Arid2 gRNA 3: GCTATGATAACAGTGTCTG	This paper	N/A
non-targeting gRNA 1: GTATTACTGATATTGGTGGG	This paper	N/A
Recombinant DNA		
WT Smarca4-sfGFP (sfGFP-Brg1)	The Crabtree Laboratory	Cat# 107056; RRID: Addgene_107056
pSG141-FLAG-Smarcc2 WT	This paper	N/A
pSG141-FLAG-Smarcc2 S586A	This paper	N/A
pSG141-FLAG-Smarcc2 S586E	This paper	N/A
CAG-IRES-GFP	Wu et al. ^{16,72}	N/A
lentiCRISPR v2	Addgene	Cat# 52961; RRID: Addgene_52961
psPAX2	Addgene	Cat# 12260; RRID: Addgene_12260
pMD2.G	Addgene	Cat# 12259; RRID: Addgene_12259
Software and algorithms		
Adobe Creative Cloud	Adobe	https://www.adobe.com/creativecloud.html
Rstudio	RStudio	https://www.rstudio.com/
Python	Python Programming Language	https://www.python.org/
Image Studio	LICORbio	https://www.licorbio.com/image-studio
SnapGene	Dotmatics	https://www.snapgene.com/
Geneious	Geneious	https://www.geneious.com/
Prism	GraphPad Software	https://www.graphpad.com/
fastQC	The Babraham Institute	https://www.bioinformatics.babraham.ac.uk/projects/fastqc/
deeptools	Ramirez et al. ⁸¹	N/A
DEseq2	Love et al. ⁸²	N/A
Kallisto	Bray et al. ⁸³	N/A
Enrichr	Chen et al. ⁸⁴	N/A
PANTHER	Mi et al. ^{85,86}	N/A
Cutadapt	Martin et al. ⁸⁷	N/A
trim_galore	The Babraham Institute	https://github.com/FelixKrueger/TrimGalore
Picard	Broad Institute	https://broadinstitute.github.io/picard/
macs2	Zhang et al. ⁸⁸	N/A
HOMER	Heinz et al. ⁸⁹	N/A
bedtools	Quinlan et al. ⁹⁰	N/A
ChrAccR	The Greenleaf Laboratory	https://greenleaflab.github.io/ChrAccR/articles/overview.html
chromVAR	Schep et al. ⁵³	N/A

(Continued on next page)

Continued

REAGENT or RESOURCE	SOURCE	IDENTIFIER
TOBIAS	Bentsen et al. ⁴⁹	N/A
samtools	Li et al. ⁹¹	N/A
SNT	Arshadi et al. ⁹²	N/A
MSconvert	Chambers et al. ⁹³	N/A

EXPERIMENTAL MODEL AND STUDY PARTICIPANT DETAILS

Animal Husbandry

In all animal experiments, mice used were wild-type CD-1 outbred mice, housed at Stanford up to 5/cage in a colony with a 12-hour light/dark cycle (lights from 7:00 am to 7:00 pm) at constant temperature (23°C) with ad libitum access to water and food. For mouse neuron cultures, embryonic day 16.5 (E16.5) male and female mouse embryos were prepared from adult CD-1 wild-type females. Animal protocols were approved by IACUC at Stanford University.

Mouse Embryonic Fibroblast (MEF) cell culture

Mouse embryonic fibroblasts were generated from F2 pups at E16.5 according to established procedure in Hathaway et al.⁹⁴ and immortalized with SV40 T antigen. MEFs were cultured in DMEM + 10% FBS + 1x penicillin-streptomycin and incubated at 37°C/5% CO₂. Cultures were passaged by trypsinization and were used before passage 10. Cultures were routinely checked for mycoplasma and immediately checked upon suspicion. No cells tested positive.

HEK293T Cell Culture

HEK293T cells (Clontech #632180) were cultured in DMEM + 10% FBS + 1x penicillin-streptomycin and incubated at 37°C/5% CO₂. Cultures were passaged by trypsinization and were used before passage 10. Cultures were routinely checked for mycoplasma and immediately checked upon suspicion. No cells tested positive.

Primary Neuron Culture

Coating plates

Culture plates (Corning #353003) were coated overnight at room temperature by flooding with poly-D-lysine (Sigma #P6407) at 0.1 mg/mL in borate buffer (1.55 g boric acid/2.4 g sodium tetraborate in 500 mL sterile water). Plates were washed 3x with water and 1x with PBS before plating neurons.

Dissection and culture

Cortical neurons were dissected and cultured following established protocols.^{4,95} Pregnant female mice were anesthetized with isoflurane and euthanized by cervical dislocation on E16.5. A 4 cm long, V-shaped incision was made through the derma and muscle layers of the lower abdomen just above the vaginal opening of the euthanized mouse. After pulling back skin and muscle, the uterus was carefully disconnected and the string of embryos gently pulled from the abdomen and placed in a dish of sterile PBS on ice. Fetuses were removed from the amniotic sac using forceps and baby scissors and placed in a second dish of fresh PBS on ice. From this point onwards, the cortex from each embryo was considered a biological replicate. Individual embryos were transferred on sterile filter paper in ice cold PBS and stabilized from behind the neck using a curved forcep. Using a sharp pair of forceps, two incisions were made: above the olfactory bulbs between the eyes and upwards between the hemispheres skimming along the underside of the skull. The flat side of a curved forcep was then used to apply gentle pressure from the brainstem to the eyes to push the brain out of the skull. The brain was scooped up and placed in a fresh dish of sterile PBS on ice. The brain was anchored vertically under a dissecting microscope by grasping near the brainstem using forceps. The meninges and remaining olfactory bulb were removed by gently tugging along the length of the tissue. Using forceps, each hemisphere was gently lifted, avoiding the hippocampus, striatum and basal ganglia, and transferred to a 15 mL sterile Falcon tube of ice-cold PBS and allowed to settle. Then, cortices were enzymatically dissociated to single neurons with Neural Tissue Dissociation Kit (P) (Miltenyi Biotech #130-092-628). Neurons were resuspended in plating media [DMEM (Life Technologies #11960-077), 10% FBS (Omega #FB-01), 1x penicillin-streptomycin (ThermoFisher #15140122)], counted, and plated at a density of 25-30M neurons per 15 cm plate, 6-10M per 10 cm plate, 1M per well of a 6-well plate, 0.5M per well of a 12-well plate, or 0.1M per well of a 24-well plate. After incubation for 1 hour at 37°C/5% CO₂, neurons were attached to the plates and media was changed to neuron maintenance media [Neurobasal Medium (Life Technologies #21103049), 2.5% B27 (ThermoFisher #17504044), 1% penicillin-streptomycin (Life Technologies #15070-063), 0.25% GlutaMax (Life Technologies #35050061)]. On day in vitro 2 (DIV2), ara-c (Sigma #C1768) was added to a final concentration of 0.5 µM to inhibit proliferation of any contaminating glial cells. Beginning on DIV3, half the media was exchanged for fresh neuron maintenance media every three days. Cultures were kept at 37°C/5% CO₂. See Figure S1E for a representative immunofluorescence staining of neuron-specific tubulin (Tuj1) in neuronal cultures.

METHOD DETAILS**MEF Serum Stimulation**

MEFs were serum starved in 0.5% FBS for 24 hours before stimulation with serum up to a final concentration of 15% for indicated time points using an established protocol.¹² Stimulation was stopped by immediate movement of the cultures to ice, washing with ice-cold PBS plus 10mM sodium butyrate to inhibit histone deacetylases, 1mM sodium orthovanadate, and 1:1000 v/v protease inhibitor cocktail (chymostatin, Millipore #230790; leupeptin, Millipore #108975; pepstatin, Millipore #516481) and 1 phosphatase inhibitor tablet/10 mL (PhosSTOP, Roche #4906837001), and harvesting by scraping with a cell lifter. Cells were pelleted at 300g for 5 mins at 4°C, flash-frozen in liquid nitrogen, and saved at -80°C until use.

Membrane Depolarization by KCl Stimulation in Neurons

At the designated DIV, neurons were silenced overnight with 1 μM tetrodotoxin (Tocris #1069) and 100 μM D-AP5 (Tocris #79055-68-8) to reflect the resting state⁹⁵ and then depolarized with 50 mM KCl for indicated time points as described.⁹⁵⁻⁹⁷ Briefly, to avoid excitotoxic death, depolarization proceeded as follows: 3/10th of neuronal media was reserved and charged with 170 mM KCl, 2 mM CaCl₂, 1 mM MgCl₂, and 10 mM HEPES pH 7.9 by adding 69.72 μL/1 mL reserved media of concentrated isotonic stimulation buffer (2.44M KCl, 28.7 mM CaCl₂, 14.4 mM MgCl₂, and 143.4 mM HEPES pH 7.9). At this point, the reserved media contains 3x the final concentration for the neuron. Control wells underwent media removal without addition of any components. The mix was restored to each well and gently swirled for 3 seconds, then the plate was placed back in the incubator for the appropriate incubation time. The excitotoxicity-induced gene *C1ca1* was verified not to be upregulated in our RNA-seq datasets, excluding toxic reaction. Neurons were then immediately moved to ice, media was then immediately exchanged to ice-cold PBS and harvested for downstream assays.

Other Pharmacological Treatments in Neurons**Inhibition of intracellular calcium signaling**

Calcium-activated signaling inhibitors were chosen to inhibit canonical calcium-activated kinase signaling pathways at their kinases closest to the nucleus that have been identified, and have specific, cell-permeable, small molecule inhibitors. The following compounds and concentrations were used: CaMKK: STO-609, 3 μM; MEK1/2i: PD0325901, 3 μM; DCLKi: DCLK-IN-1, 2.5 μM; CaNi: 10 nM FK506 + 1 μM cyclosporin (CsA). Cyclosporin A and FK506 were used together because of the greater abundance of calcineurin in neurons compared to FKBP and cyclophilin, which are required for formation of inhibitor complexes.³⁰ Inhibitors were given at a final concentration of 0.1% DMSO for a 30 mins pre-treatment before depolarization or unstimulated for the indicated times (30 mins or less).

Inhibition of BAF ATPase activity

FHT1015 was obtained as lyophilized powder as a kind gift from Steve Bellon, Foghorn Therapeutics. A final concentration of 100 nM FHT1015 or DMSO at final 0.1% DMSO concentration was added to reserved neuronal media during depolarization or in the resting unstimulated state and added back to wells. The concentration was chosen from the reported biochemical *in vitro* IC₅₀ of inhibition of BAF ATPase activity as compared to other remodelers.

Lentivirus Production

Lentivirus was produced using a previously described protocol⁹⁸ from a 15 cm plate of 25M lenti-x HEK293T cells (Clontech #632180) via polyethylenimine (PEI) transfection, using lentiviral constructs and packaging plasmids psPAX2 and pMD2.G. Two days after transfection, the media containing the virus was collected, filtered with a 0.4 μM filter, and ultra-centrifuged for 2 hours at 20,000 rpm in an SW28 rotor (Beckman). Relative titer was estimated by Lenti-X GoStix Plus (Takara #631280) and was similar for all viral constructs. Viral pellets were resuspended in 250 μL PBS and flash-frozen.

CRISPR Constructs

CRISPR knockout constructs were constructed using lentiCRISPR v2 (a gift from Feng Zhang, Addgene plasmid # 52961; <http://n2t.net/addgene:52961>; RRID:Addgene_52961) using gRNAs targeting isoform-conserved exons in mouse *Smarcc2/Baf170* and *Arid2/Baf200*. 3 gRNAs were designed using CRISPRick⁹⁹ and pooled virus was made from the 3 lentiCRISPR v2 plasmids at equimolar ratios. Target sequences for *Smarcc2* were: (1) GCGTCCATGCCATTGAACGG; (2) ACACCGACACATTCAACGAG; and (3) GACAG GATACACAACATGGG. Target sequences for *Arid2* were (1) ACTTGCAGTAAATTAGCTCG; (2) GAGGATAAGCTGCCCCCTG; and (3) GCTATGATAACAGTGTCTTG. The non-targeting control sequence was GTATTACTGATATTGGTGGG.

Lentiviral Overexpression Constructs

Smarcc2 (ENSMUSP00000096734) overexpression constructs were subcloned from *Smarcc2* cDNA published previously.⁵⁹ Among *Smarcc2* isoforms annotated, the transcript encoding this isoform (ENSMUST00000099131) was the highest expressed in our RNA-seq data from cortical E16.5 neurons (average transcripts/million (TPM): 103) and the corresponding protein (Uniprot: Q3UID0) was also the primary isoform expressed in our proteomic dataset. To create lentiviral overexpression constructs, first, a wild-type (WT) overexpression construct was subcloned into pUC19 and wobbled at PAM sites targeted by the *Smarcc2* gRNAs using site-directed

mutagenesis (NEB #E0554S) (renamed pSG141). Further site-directed mutagenesis was performed to generate point mutants at phospho-sites of interest. The constructs were then subcloned into an EF1a-driven lentiviral vector containing a blasticidin resistance gene driven by a PGK promoter. The final open-reading frame codes for an N-terminal FLAG tag followed by wobbled Smarcc2 that is wild-type or contains point mutations at indicated phosphosites. A lentiviral vector encoding an empty open-reading frame was used as a negative control in experiments. All constructs were verified using Sanger sequencing. Brg1-sfGFP was a gift from Jerry Crabtree & Courtney Hodges (Addgene plasmid # 107056; <http://n2t.net/addgene:107056>; RRID: Addgene_107056).

Lentiviral Transduction of Neurons

Smarcc2 knockout and overexpression

Titer was estimated from infection of HEK293T cells and selection with puromycin (1 µg/mL) and blasticidin (0.75 µg/mL). On DIV4, concentrated virus was added to primary neurons. The relevant CRISPR knockout and Smarcc2 overexpression or empty vector constructs were pooled 1:1 (v:v). 10 µL of total virus was applied to one well of a 12-well plate of 0.5M neurons/well and 20 µL was applied to one well of a 6-well plate of 1M neurons/well. Media changes and neuronal culture proceeded as normal. Neuronal culture is sensitive to antibiotic selection and thus assays were performed after 14 days of infection (on DIV18) to allow time for overexpression. This time point was chosen from empirical data for overexpression efficiency in neurons and validated by Western Blot (Figure S5E).

Arid2 knockout

Titer was estimated from infection of HEK293T cells and selection with puromycin (1 µg/mL). On DIV3, concentrated virus was added to primary neurons. 25 µL of total virus was applied to one well of a 6-well plate of 1M neurons/well. Media changes and neuronal culture proceeded as normal. Cells were treated with indicated conditions (e.g., depolarization) and harvested for assays on DIV7.

Nuclear Extract Preparation

A 15 cm plate of neurons or fibroblasts was washed 1x with 10 mL ice cold PBS supplemented with 10mM sodium butyrate to inhibit histone deacetylases, 1mM sodium orthovanadate, and 1:1000 (v:v) protease inhibitor cocktail (chymostatin, Millipore #230790; leupeptin, Millipore #108975; pepstatin, Millipore #516481) and 1 phosphatase inhibitor tablet/10 mL (PhosSTOP, Roche #4906837001). Cells were lifted with a cell lifter and pelleted at 2,000g for 5 mins at 4°C. Pellets were flash-frozen and stored until further processing.

Low-salt/benzonase extraction of soluble nuclear protein

After thawing on ice, cell pellets were washed once more with 10 mL cold PBS supplemented with 10mM sodium butyrate, 1mM sodium orthovanadate, and protease and phosphatase inhibitors (hereafter: PBS*) and resuspended in NE10 buffer (20 mM HEPES (pH 7.5), 10 mM KCl, 1 mM MgCl₂, 0.1% Triton X-100 (v/v), protease inhibitors (Roche), 15 mM β-mercaptoethanol), dounced 15 times and pelleted. Nuclei were washed in NE10 buffer and then digested with 250 units benzonase (Millipore) for 30 mins rotating at 25°C. Nuclei were resuspended in NE150 buffer (NE10 supplemented with 150mM NaCl) and incubated for 20 mins. Lysates were pelleted at 16,000 g for 20 mins at 4 °C and supernatants were taken for gradient or immunoprecipitation analysis. The concentration of protein in the supernatant was measured by Bradford.

Ammonium sulfate precipitation of chromatin from nuclei

After thawing on ice, cell pellets were washed once more with 10 mL cold PBS plus 10mM sodium butyrate, 1mM sodium orthovanadate, and protease and phosphatase inhibitors (hereafter: PBS*) and resuspended in 250 µL Buffer A (25mM HEPES pH 7.5, 25mM KCl, 5mM MgCl₂, 10% glycerol (v/v), 0.1% NP-40 (v/v)) supplemented with 10mM sodium butyrate, 1mM sodium orthovanadate, and protease and phosphatase inhibitors (hereafter: Buffer A*), incubated for 7 mins on ice, and an aliquot taken to count nuclei using Trypan Blue and a hematocytometer. Nuclei were pelleted at 500g for 5 min at 4°C, and the supernatant saved as the cytosolic fraction. If nuclei purity was not > 90%, the Buffer A* incubation was repeated. Nuclei were washed with 5 mL Buffer C (10mM HEPES pH 7.5, 100mM KCl, 2mM MgCl₂, 10% glycerol (v/v), 0.5mM CaCl₂) supplemented with 10mM sodium butyrate, 1mM sodium orthovanadate, and protease and phosphatase inhibitors (hereafter: Buffer C*). Nuclei were finally resuspended in 700 µL Buffer C* and chromatin was precipitated by slow dropwise addition of 108 µL 3M ammonium sulfate (final: 0.4M) and rotation at 4°C for 1 hour. Chromatin was pelleted by ultracentrifugation in polyallomer centrifuge tubes (Beckman #343778 11x34mm) at 100,000 rpm for 15 mins at 4°C and the supernatant was saved. The concentration of protein in the supernatant was measured by Bradford.

Preparation of nuclear protein for whole nuclear proteomics

After nuclear extraction and chromatin precipitation with ammonium sulfate as above, supernatant (in Buffer C*) was precipitated by 1:4 (v:v) addition of trichloroacetic acid (TCA), vortexing and incubation on ice for 30 mins, pelleting by centrifugation at 16,000 g for 15 mins at 4°C, washing 1x with 1 mL ice-cold acetone, and finally washing 2x with 1 mL ice-cold methanol. Pellets containing denatured protein were stored at -80°C until ready for MS sample processing. For SDS-PAGE analyses, nuclear extracts were equalized in protein concentration and denatured in 1X NuPage LDS/RIPA sample buffer (Thermo NP0008) supplemented with 1mM DTT by incubation at 95 °C for 5 mins.

Preparation of nuclear protein for immunoprecipitation and gradient experiments

After nuclear extraction and chromatin precipitation with ammonium sulfate as above, 233 mg of solid ammonium sulfate was added to the 805 µL of supernatant (in Buffer C*) (final: 2.18M at 4°C; ~50% saturation¹⁰⁰) and resuspended well, then incubated on ice for 30 minutes with mixing every 10 minutes. BAF complexes and other nuclear proteins were precipitated by ultracentrifugation at 100,000 rpm for 15 mins at 4°C and the pellet was saved at -80°C until immunoprecipitation. Protein precipitation is due to increase

in surface tension of water by ammonium sulfate that reduces solubility and favors folding, as opposed to a chaotropic (“salting-in”) mechanism of precipitation that causes denaturation.¹⁰⁰ Hence, this method enables ready resolubilization of protein for downstream assays in any chosen buffer. The saturation percentage chosen was empirical and is useful to purify large multiprotein complexes as well as smaller transcription factors, including RSC and SAGA,¹⁰¹ RNA polymerase II,¹⁰² BAF from the brain,¹⁰³ and TMPRSSERG.¹⁰⁴ Recovery of BAF subunits in extracts from the procedure is almost 90% as shown in Figure S2A and S2B.

Immunoprecipitation (IP) from Neurons

BAF IP-Mass spectrometry (MS)

Soluble nuclear protein was resuspended in 205 µL IP Buffer (20mM HEPES pH 7.5, 150 mM KCl, 1mM MgCl₂, 0.5mM CaCl₂, 10% (v/v) glycerol, 0.1% (v/v) Triton X-100) supplemented with 10mM sodium butyrate, 1mM sodium orthovanadate, and protease and phosphatase inhibitors (hereafter: IP Buffer*) and concentration was measured by Bradford. Extracts were normalized by total protein concentration and identical amounts of total protein and concentration were used for IP in each condition (256 µg per IP at 0.86 µg/µL). 3.1% (8 µg) was saved as input. 5 µg anti-Brg1 antibodies (SantaCruz H-10) or normal mouse IgG (Santa Cruz sc-2025) crosslinked to Protein G Dynabeads (Invitrogen #10003D) using BS3 (bis(sulfosuccinimidyl)suberate) (ThermoFisher #A39266) were added to samples and incubated with overnight rotation at 4 °C. 5 µg antibody was incubated with rotation at room temperature to 50 µL Protein G beads, washed 2X with 1 mL PBS and 2X with 1 mL Conjugation Buffer (20mM sodium phosphate, 150mM NaCl pH 8.0), then incubated with 230 µL of 2.86 mg/mL BS3/Conjugation Buffer for 30 mins exactly at RT under rotation, quenched with 12.5 µL 1M Tris pH 7.5 with 15 mins rotation at RT, and washed 2X with IP*. IPs were washed 3X the next day with 1mL IP Wash* (IP* except 300mM KCl instead of 150mM KCl) and eluted with a low-pH/glycine protocol: beads were resuspended in 50 µL 0.1M glycine-HCl pH 2.5, incubated with shaking at 900 rpm for 30 mins at 37 °C, centrifuged briefly then supernatant was transferred to a new tube on ice and neutralized with 5 µL 1M Tris pH 8, and repeated once. 10% was run on a gel to confirm the IP. The remaining 90% elute was precipitated by 1:4 (v:v) addition of trichloroacetic acid (TCA), vortexing and incubation on ice for 30 mins, pelleting by centrifugation at 16,000 g for 15 mins at 4 °C, washing 1x with 1 mL ice-cold acetone, and finally washing 2x with 1 mL ice-cold methanol. Pellets containing denatured protein were stored at -80 °C until ready for MS sample processing.

IP for immunoblot

Soluble nuclear protein was resuspended in 205 µL IP Buffer (20mM HEPES pH 7.5, 150 mM KCl, 1mM MgCl₂, 0.5mM CaCl₂, 10% (v/v) glycerol, 0.1% (v/v) Triton X-100) containing 10mM sodium butyrate to inhibit histone deacetylases, 1mM sodium orthovanadate, and protease and phosphatase inhibitors (hereafter: IP Buffer*) and concentration was measured by Bradford. Extracts were normalized by total protein concentration and identical amounts of total protein and concentrations were used for IP in each condition (50-200 µg at 0.25-1 µg/µL). 1-10% (v/v) was saved as input. 1-3 µg anti-Smarcc2/Baf170 antibodies (homemade,⁵⁹ rabbit polyclonal, recognizes conserved internal epitope centered in Ile818) or normal rabbit IgG (Cell Signaling 2729) and Protein G Dynabeads (Invitrogen #10003D) were added to samples and incubated with rotation overnight at 4 °C. The IP was cross-validated using immunoblot against the same bait but with a different antibody: anti-Smarcc2 (SantaCruz monoclonal mouse E-6). Samples were washed five times with 1 mL IP Buffer* and eluted by denaturation in 1X NuPage LDS/RIPA sample buffer (Thermo NP0008) supplemented with beta-mercaptoethanol by incubation at 95 °C for 5 mins.

Immunoprecipitation from HEK293T Cells

HEK293T cells were transfected with sfGFP-Brg1 and FLAG-Smarcc2 constructs using polyethylenimine (PEI) and harvested after 24-48 h. Cells were lysed in NE10 buffer (20 mM HEPES (pH 7.5), 10 mM KCl, 1 mM MgCl₂, 0.1% Triton X-100 (v/v), protease inhibitors (Roche), 15 mM β-mercaptoethanol), dounced 15 times and pelleted 5 mins at 500 g. Nuclei were washed in NE10 buffer and then digested with 250 units benzonase (Millipore) for 30 mins rotating at 25 °C. Nuclei were resuspended in NE150 buffer (NE10 supplemented with 150mM NaCl) and incubated for 20 mins. Lysates were pelleted at 16,000 g for 20 mins at 4 °C and supernatants were immunoprecipitated by incubating 2.5ug anti-FLAG antibodies (F1804, Millipore-Sigma) and Protein G Dynabeads (Invitrogen #10003D) overnight at 4 °C. The IP fraction was recovered by magnetic separation. Samples were washed three times with 1 mL NE150 and eluted by denaturation in 1X NuPage LDS sample buffer (Thermo NP0008) supplemented with beta-mercaptoethanol by incubation at 95 °C for 5 mins.

Glycerol Gradient

Glycerol gradients (10-30%) of nuclear proteins were carried out as previously established.¹⁰³ Briefly, precipitated neuronal or MEF nuclear protein from ammonium sulfate-precipitated extracts was resuspended in ice-cold HEMG-0 buffer (50 mM HEPES pH 7.9, 100mM KCl, 0.1 mM EDTA, 12.5 mM MgCl₂) supplemented with 1mM sodium orthovanadate, 10mM sodium butyrate, and protease and phosphatase inhibitors (hereafter: HEMG-0*). For nuclear extracts prepared with low-salt/bezonase buffer treatment, the solubilized protein in NE10 buffer (20 mM HEPES (pH 7.5), 10 mM KCl, 1 mM MgCl₂, 0.1% Triton X-100 (v/v), protease inhibitors (Roche), 15 mM β-mercaptoethanol) was used directly. 2.5% (v/v) was reserved as input. A 10-30% gradient of glycerol in HEMG buffer (v/v) was poured into 14 x 89 mm polyallomer centrifuge tubes (Beckman #331372). The resuspended nuclear extract was carefully layered on top of the gradient and centrifuged in an SW41 rotor at 40,000 rpm for 16 hours at 4 °C. Twenty 500 µL fractions were collected carefully, without disturbing the gradient, and each fraction was TCA/acetone precipitated by adding 1:4 (v:v) of trichloroacetic acid (TCA), vortexing and incubating on ice for 30 mins, pelleting by centrifugation at 16,000g for 15 mins at 4 °C, washing 1x

with 1 mL ice-cold acetone, and finally washing 2x with 1 mL ice-cold methanol. Fractions were then resuspended in 1X NuPage LDS sample buffer (Thermo NP0008) supplemented with beta-mercaptoethanol, denatured at 95 °C for 5 mins, and run on SDS-PAGE gels. Proteins were transferred at constant 85 mA, 4 °C overnight to PVDF membranes and blotted using antibodies to subunits of the BAF complex or other controls. For comparisons between distributions in gradient experiments, the two-sample Wasserstein distance test was used using the “wass_test” function in the R package *twosamples*.

Sample Processing for Quantitative TMT-Proteomic Analysis

Samples were prepared following the SL-TMT protocol.¹⁰⁵ A total of 100 µg of protein from each nuclear extract sample (for whole nuclear extract MS proteomics) or the elute from the Brg1 immunoprecipitation (for the BAF IP-MS) was used. Reduction of sample (5 mM TCEP for 15 min.) was followed by alkylation (10 mM iodoacetamide for 30 min.) and quenching (5 mM DTT for 15 min.). Samples were then chloroform-methanol precipitated. The precipitated proteins were resuspended in 200 mM EPPS pH 8.5, digested first by Lys-C overnight at room temperature and later by trypsin (6 h at 37 °C). Both enzymes were used at a 1:100 enzyme-to-protein ratio.

The samples were then labeled with tandem mass tag (TMTpro) reagents.¹⁰⁵ Acetonitrile was added to a final volume of 30% prior to adding the TMTpro labeling reagent. For protein level analysis, ~50 µg of peptides were labeled with 100 µg of TMT. For phosphopeptide analysis, we estimated the phosphopeptide enrichment to be ~1.5:100 and so ~30 µg of peptides were labeled with 60 µg of TMT. Labeling occurred at room temperature for 1 h. Once labeling efficiency was verified (here, >97%), hydroxylamine was added at a final concentration of ~0.3% and incubated for 15 min at room temperature and the samples were pooled at a 1:1 ratio across all channels.

To enrich phosphopeptides, the pooled sample was desalted over a 200 mg SepPak column and phosphopeptides were enriched with the Pierce High-Select Fe-NTA Phosphopeptide enrichment kit following manufacturer’s instructions. The eluate was desalted via StageTip¹⁰⁶ and was ready for MS analysis. The washes and the unbound fraction of this enrichment were desalted and used for proteome-level analysis.

For whole nuclear extracts and BAF IPs, the pooled samples were desalted by solid phase extraction (100 mg SepPak column) and fractionated using basic-pH reversed-phase (BPRP) Liquid Chromatography using an Agilent 1200 pump with an Agilent 300Extend C18 column (2.1 mm ID, 3.5 µm particles, and 250 mm in length). The flow rate over the column was 0.25 mL/min and we used 50-min linear gradient with 5% to 35% acetonitrile in 10 mM ammonium bicarbonate pH 8. Ninety-six fractions were collected and concatenated into 24 superfractions prior to desalting.¹⁰⁷ These 24 superfractions were sub-divided into two groups, each consisting of 12 non-adjacent superfractions. These superfractions were subsequently acidified with 1% formic acid and vacuum centrifuged to near dryness. Each superfraction was desalted via StageTip.¹⁰⁶ Once dried by vacuum centrifugation, the sample was reconstituted using 5% formic acid and 5% acetonitrile prior to acquisition of LC-MS/MS data.

Mass Spectrometry Data Collection and Processing

Mass spectrometric data were collected on an Orbitrap Fusion Lumos mass spectrometer, both which are coupled to a Proxeon NanoLC-1200 UHPLC and a FAIMSpro interface.¹⁰⁸ The 100 µm capillary column was packed with 35 cm of Accucore 150 resin (2.6 µm, 150 Å; ThermoFisher Scientific).

Mass spectrometric data for whole nuclear extracts were collected on Orbitrap Fusion Lumos instruments (using RTS-MS3) coupled to a Proxeon NanoLC-1200 UHPLC. The 100 µm capillary column was packed with 35 cm of Accucore 150 resin (2.6 µm, 150 Å; ThermoFisher Scientific) at a flow rate of 565 nL/min. The scan sequence began with an MS1 spectrum (Orbitrap analysis, resolution 60,000, 400–1600 Th, automatic gain control (AGC) target 100%, maximum injection time “auto”). Data were acquired ~90 minutes per fraction. MS2 analysis consisted of collision-induced dissociation (CID), quadrupole ion trap analysis, automatic gain control (AGC) 100%, NCE (normalized collision energy) 35, q-value 0.25, maximum injection time 35ms), and isolation window at 0.7 Th. RTS was enabled and quantitative SPS-MS3 scans (resolution of 50,000; AGC target 2.5x105; collision energy HCD at 55%, max injection time of 250 ms) were processed through Orbiter with a real-time false discovery rate filter implementing a modified linear discriminant analysis. For FAIMS, the dispersion voltage (DV) was set at 5000V, the compensation voltages (CVs) used were -40V, -60V, and -80V, and -30V, -50V, and -70V, and the TopSpeed parameter was set at 1 sec.

For IP-MS profiling, data were acquired using multiple injections (n=6) on an Orbitrap Eclipse mass spectrometer with varying combinations of FAIMS CVs between -30 and -80V (3 CVs per set) over a 150 min gradient. A 1sec TopSpeed cycle was used for each CV. The scan sequence began with an MS1 spectrum (Orbitrap analysis, resolution 60,000, 400-1500 Th, automatic gain control (AGC) target 100%, maximum injection time “auto”). Data were acquired ~90 min per fraction. The hrMS2 stage consisted of fragmentation by higher energy collisional dissociation (HCD, normalized collision energy 36%) and analysis using the Orbitrap (AGC 300%, maximum injection time 200 ms, isolation window 0.5 Th, resolution 50,000).

For phosphopeptide profiling, data were acquired using three to five injections on an Orbitrap Eclipse mass spectrometer with varying combinations of FAIMS CVs between -30 and -80V (3 CVs per set) over a 150 min gradient. A 1sec TopSpeed cycle was used for each CV. The scan sequence began with an Orbitrap MS1 spectrum with the following parameters: resolution: 120,000, scan range: 400-1500 Th, automatic gain control (AGC): 100%, and maximum injection time: “auto.” MS2 analysis consisted of higher-energy collisional dissociation (HCD) with the following parameters: resolution: 50,000, AGC: 300%, normalized collision

energy (NCE): 36%, maximum injection time: 250 ms, and isolation window: 0.5 Th, and. In addition, unassigned, singly, and > 5+ charged species were excluded from MS2 analysis and dynamic exclusion was set to 60 s.

Once the spectra were converted to mzXML using MSconvert,⁹³ database searching could be performed. Database searching included all mouse entries from UniProt (downloaded March 2021), which was concatenated with a version of the database in which the order of the amino acid residues of each protein was reversed. Database searches used a 50-ppm precursor ion tolerance and a product ion tolerance of 0.03 Da for hrMS data. RTS-MS3 data used a 0.9 Da product ion tolerance.^{109,110} For static modifications, lysine residues and peptide N-termini were modified with +304.207 Da due to the TMTpro labels and +229.162 Da for classic TMT (IP-MS only). Meanwhile, all cysteine residues were modified with iodoacetamide (carbamidomethylation) that results in a +57.021 Da increase in mass. Also, methionine oxidation (+15.995 Da) was set as a variable modification. Likewise, deamidation (+0.984 Da) at glutamine and asparagine residues and phosphorylation (+79.966 Da) at serine, threonine, and tyrosine residues were also set as variable modifications for phosphopeptide enrichment. The false discovery rate (FDR) was set at 1% at the peptide level with filtering a linear discriminant analysis.¹¹¹ The protein lists were assembled further to a final protein-level FDR of 1%. The intensities of reporter ions were corrected for the isotopic impurities of the different TMT reagents.¹¹² For each protein, the peptide summed signal-to-noise (S/N) measurements were summed and normalized to account for equal protein loading by equating the sum of the signal for all proteins in each channel. For phosphosite identification, the AScore¹⁰⁹ false-discovery metric was used and only phosphosites that were “high-confidence”, with $p \leq 0.05$, were retained. Students' t-test was used for differential site and protein pull-down calling. Human keratin and other contaminants were manually excluded from downstream analyses. A summary of the BAF IP-MS and phosphoproteomic data is as follows: contaminant peptides (e.g., KRT, TRY): 2%; unique proteins detected: 1,637; unique BAF subunits detected: 28; unique phosphosites detected: 583; unique phosphosites on BAF subunits detected: 37; bait (Brg1) peptides detected: 709.

Western Blotting

Cells were harvested on ice in RIPA buffer (50mM Tris-HCl pH 8, 150mM NaCl, 1% NP-40, 0.1% DOC, 1% SDS, protease inhibitor cocktail (chymostatin, Millipore #230790; leupeptin, Millipore #108975; pepstatin, Millipore #516481), 1mM MgCl₂, 1mM DTT) and 1:200 benzonase (Sigma #E1014) was added and incubated for 20 mins at room temperature. After 10 min centrifugation at 14,000g and 4°C, the supernatant was collected and protein concentration was measured by Bradford. Antibodies used for immunoblots were: Brg1 (1:1000 (v:v), Santa Cruz H-10), Smarcc2/Baf170 (1:1000, homemade,⁵⁹ rabbit polyclonal, recognizes conserved internal epitope centered in Ile818), Smarcc2 (1:1000, SantaCruz mouse monoclonal E-6), Smarcb1/Ini1/Baf47 (1:1000, Santa Cruz A-5), Vinculin (1:1000, ThermoFisher 700062), CREST (1:1000, SantaCruz D-7), Hdac1 (1:1000, Cell Signaling 10E2), FLAG (1:1000, Millipore F1804), GFP (1:1000, Invitrogen A6455), Pbrm1/Baf180 (1:1000, homemade rabbit polyclonal^{67,113,114}), Phf10/Baf45a (1:500, GeneTex GTX116314), Brd7 (1:500, Santa Cruz B-8), Arid2 (1:500, Santa Cruz E-3), β-Actin (1:2000, Cell Signaling 13E5), H3 (1:5000, abcam 1791) and Gapdh (1:2000, Santa Cruz 6C5). ImageStudio (Licor) was used for blot imaging and quantification.

RNA Extraction, qPCR, and Sequencing Library Preparation

Cells were harvested in TRIsure (Bioline #38033). RNA was extracted using Direct-zol RNA MicroPrep columns (Zymo #R2062) treated with DNaseL. cDNA was prepared for RT-qPCR using the SensiFAST cDNA preparation kit according to manufacturer instructions (Bioline #65054). 1μL of cDNA was used per RT-qPCR reaction prepared with SYBR Lo-ROX (Bioline #94020) and carried out using an Applied Biosystems QuantStudio 6Pro. *cFos* primers were from⁴: *Fos* FWD: CGGGTTCAACGCCGACTA

Fos REV: TTGGCACTAGAGACGGACAGA; *Gapdh* FWD: CTGACGTGCCGCTGGAGAAC

Gapdh REV: CCCGGCATCGAAGGTGGAAGAGT. For sequencing library preparation, rRNA was depleted (NEB #E7400) and prepared into paired-end libraries (NEB #E7760). For naïve (WT) DIV7 neuron RNA-seq, polyA-enriched mRNAs were isolated (NEB #E7490). Library size distributions were confirmed using an Agilent Bioanalyzer and High Sensitivity DNA reagents (Agilent 5067) and concentrations determined by qPCR. Equimolar pooled libraries were sequenced on an Illumina NextSeq or HiSeq.

RNA-seq Analysis

Raw reads were checked for quality using fastqc (<https://www.bioinformatics.babraham.ac.uk/projects/fastqc/>) and trimmed from adapters using cutadapt⁸⁷ using parameters cutadapt -a AGATCGGAAGAGCACACGTCTGAACCTCCAGTC -b AGATCGGAAGAGC GTCGTGTAGGGAAAGAGTGT -nextseq-trim=20 -minimum-length 1. Transcripts were quantified using kallisto⁸³ against a mouse Gencode vM24 indexed transcriptome and annotations. Transcript isoforms were collapsed to genes and differential gene analysis was performed using DESeq2⁸² using aperglm¹¹⁵ to shrink fold changes. PCA analysis was performed using DESeq2. Pathway analyses were performed using Enrichr⁸⁴ and PANTHER^{85,86} on genes defined by significance cutoffs as detailed in figure legends. Unbiased clustering analyses were performed using pheatmap¹¹⁶ including any significantly changed genes in treatment conditions compared.

ATAC-seq

ATAC-seq libraries were constructed from on-plate nuclear prep of neurons plated at 1M/6-well of a 6-well plate as described in.¹¹⁷ Briefly, DNase at a final concentration of 200 U/mL was added to wells for 30 mins at 37°C concurrent with indicated treatment timepoints (such as stimulation, and/or drug addition). Neuronal media was quickly dumped and neurons were washed 4X

with cold PBS. 1mL of RSB-Lysis buffer/well (10mM Tris pH 7.4, 10mM NaCl, 3 mM MgCl₂, 0.1% NP-40 (v/v), 0.1% Tween-20 (v/v), 0.01% Digitonin (v/v)) was added and incubated for 10 mins on ice, then nuclei were gently lifted, counted by a hematocytometer, and spun down at 500 g for 4 °C for 10 mins in a swing-bucket centrifuge. 75,000 nuclei were taken for further processing. Lysis buffer was washed out with RSB-Wash (containing 0.1% Tween-20 but no NP-40 or Digitonin). The pellet was resuspended in transposition mixture (25 µL 2X TD Buffer (20mM Tris pH 7.6, 10mM MgCl₂, 20% DMF (v/v)), 100 nM final Tn5 transposase (home-made, gift from William Greenleaf), 16.5 µL PBS, 0.5 µL 1% digitonin, 0.5 µL 10% Tween-20 (v/v), 5 µL H₂O) and incubated for 30 mins at 37 °C with 1000 rpm shaking. Reactions were cleaned up, amplified into libraries, indexed, and quantified using published protocol.⁷⁷ Library size distributions were confirmed using an Agilent Bioanalyzer and High Sensitivity DNA reagents (Agilent #5067) and concentrations determined by qPCR. Equimolar pooled libraries were sequenced on an Illumina NextSeq or NovaSeq.

ATAC-seq Analysis

ATAC-seq reads were checked for quality using fastqc (<https://www.bioinformatics.babraham.ac.uk/projects/fastqc/>) and trimmed from adapters using trim_galore (<https://github.com/FelixKrueger/TrimGalore>) with parameters -paired -nextera. Trimmed reads were aligned to the mouse mm10 genome using bowtie2 with parameters -very-sensitive -X2000. Low quality reads, duplicated reads and reads with multiple alignments were removed using samtools⁹¹ and Picard (<https://broadinstitute.github.io/picard/>). Positions of Tn5 inserts were determined as read start position offset by +4 bp for reads aligned to the + strand and as a read start position offset by -5 bp for reads aligned to the - strand. macs2⁸⁸ callpeak was used for peak calling with Tn5 insert positions and parameters -p 0.01 -nolambda -shift -75 -extsize 150 -nomodel -call-summits -keep-dup all. Bedtools⁹⁰ was used to find consensus set of peaks by merging peaks across multiple conditions (bedtools merge), count number of reads in peaks (bedtools intersect -c) and generate genome coverage (bedtools genomecov -bga). The peak differential analysis and PCA analysis was performed using DESeq2⁸² using aeglom¹¹⁵ to shrink fold changes. Motif enrichment analysis was performed on peak summits using findMotifsGenome.pl from HOMER⁸⁹ using parameters mm10 -size 200 -bg \$bgfile where \$bgfile = background of all consensus peaks detected. Variation of accessibility at transcription factor motifs was computed by summarizing count data across 200 bp window tiles using the ChrAccR suite (<https://greenleaflab.github.io/ChrAccR/articles/overview.html>) with default parameters and then calculating the Tn5-bias-corrected Z-score of accessibility across all motifs in JASPAR using chromVAR.⁵³ Footprint profiles were generated using the getMotifFootprints function in ChrAccR. TOBIAS⁴⁹ was used to compute differential footprint scores.

CUT&RUN Experiment and Library Preparation

CUT&RUN was performed as previously described^{78,79} with modifications. Briefly, neurons were plated at 1M/6-well of a 6-well plate and harvested by scraping in 1 mL PBS supplemented with protease and phosphatase inhibitors and pelleting for 3 mins at 1,200g at 4 °C. Cells were resuspended in 1 mL nuclear extraction buffer (NE: 20mM HEPES pH 7.9, 10 mM KCl, 0.1% Triton X-100 (v/v), 20% glycerol (v/v), 0.5 mM spermidine, 1X cOmplete protease inhibitors (Roche 11836153001), 1 phosphatase inhibitor tablet/10 mL (PhosSTOP, Roche #4906837001), pelleted at 1,700g for 3 mins at 4 °C, and washed twice more. Nuclei were resuspended in NE, charged with paramagnetic-bead conjugated activated Concanavalin A coated beads (EpiCypher 21-1411), and rotated for 1 hr at 4 °C. 250,000 nuclei were counted and incubated with primary antibodies at 1:50 dilution (v:v) (anti-Brg1: Santa Cruz H-10; anti-Smarcc2: Santa Cruz E-6) in antibody buffer (20mM HEPES pH 7.9, 150 mM NaCl, 0.5mM spermidine, protease and phosphatase inhibitors, 0.025% digitonin, 2 mM EDTA). Incubation proceeded for 1 hr under shaking at 1,500 rpm at 4 °C; nuclei were resuspended gently every 30 minutes. Primary antibodies were washed with wash buffer (20mM HEPES pH 7.9, 150 mM NaCl, 0.5mM spermidine, protease and phosphatase inhibitors, 0.025% digitonin) and rabbit anti-mouse IgG secondary antibodies (EMD Millipore 06-371) were added at 1:100 (v:v) dilution in antibody buffer. Incubation proceeded for 1 hr under shaking at 900 rpm at 4 °C; nuclei were resuspended gently every 30 minutes. Secondary antibodies were washed using wash buffer twice and resuspended in wash buffer charged with 1:50 (v:v) dilution of pA-MNase (a kind gift from Steve Henikoff). Incubation proceeded for 1 hr under shaking at 800 rpm at 4 °C; nuclei were resuspended gently every 30 minutes. Nuclei were washed twice with wash buffer, washed once with low salt rinse buffer (3.5 mM HEPES pH 7.9, 0.5 mM spermidine, 0.025% digitonin). After incubation in ice-cold water for 1-5 minutes to allow the temperature to reach 0 °C, digestion commenced upon addition of 10 mM CaCl₂ (final). Digestion proceeded for 5 minutes before termination by addition of stop buffer at 1:3 dilution (v:v) (4X stop buffer: 680 mM NaCl, 40 mM EDTA, 80 mM EGTA, 0.04% digitonin, 0.1 µg/µL RNaseA, 0.1 µg/µL glycogen) and incubation at 37 °C for 30 minutes to release digested DNA. The sample was centrifuged at 5,000g for 5 minutes at 4 °C and supernatant containing DNA collected. DNA was purified by phenol:chloroform extraction and size distributions were confirmed using an Agilent Bioanalyzer and High Sensitivity DNA reagents (Agilent 5067). Libraries were prepared following described protocol to make libraries from small DNA fragments¹¹⁸ (<https://doi.org/10.17504/protocols.io.wvgfe3w>); briefly: Paired-end sequencing libraries were constructed using an NEBNext Ultra II DNA kit (E7645S) and indexed (NEB E7335). Libraries were size-selected using Ampure XP beads (Beckman A63882). Library size distributions were confirmed using an Agilent Bioanalyzer and High Sensitivity DNA reagents (Agilent 5067) and concentrations determined by qPCR. Equimolar pooled libraries were sequenced on an Illumina HiSeq with 2 x 150 bp cycles.

CUT&RUN Analysis

The data quality was checked using fastq (<https://www.bioinformatics.babraham.ac.uk/projects/fastqc/>). The raw reads were trimmed from adapters with cutadapt (parameters: -a AGATCGGAAGAGCACACGTCTGAACTCCAGTCA -A AGATCGGAAGAGCGTCGTAGGGAAAGAGTGT) and raw reads were aligned to mm10 mouse genome assembly using bowtie2 (parameters: -local -maxins 1000). Low quality reads, duplicated reads and reads with multiple alignments were removed using samtools⁹¹ and Picard (<https://broadinstitute.github.io/picard/>). deepTools⁸¹ was used to generate coverage densities across multiple experimental conditions (deepTools computeMatrix and deepTools plotProfile) and to generate bigwig files (deepTools bamCoverage), where reads mapping to ENCODE blacklist regions were excluded.¹¹⁹ All metaprofiles shown were calculated with sequence-depth-normalized, replicate-merged (bigWigMerge¹²⁰).

Activity-dependent Dendritic Outgrowth Experiment and Analysis

Activity-dependent dendritic outgrowth was studied using established protocol in.¹⁶ After dissection, cortical neurons were nucleofected (Lonza #VPG-1001) with knockout, vector control, or overexpression constructs, along with a GFP¹⁶ construct to enable visualization, and plated at 50,000/well on poly-D-lysine-coated 24-well glass plates (Cellvis #P24-1.5H-N). Identical quantities by mass of DNA/cells were added for each construct. On DIV4, wells were stimulated with 30 mM KCl for 18 hours or silenced with D-AP5/TTX. The next day, neurons were washed 1X with PBS by incubation for 5 mins at RT, fixed in 4% (v/v) paraformaldehyde (PFA), washed 1X in PBS, permeabilized with 0.3% Triton-X-100/PBS (v/v) for 15 mins at RT, washed 3X with PBS, blocked with 2.5% normal donkey serum (Jackson ImmunoResearch #005-000-121)/2.5% normal goat serum (Jackson ImmunoResearch #017-000-121)/1% (v/v) BSA for 1 hour at RT, then stained with 1:2000 chicken anti-GFP (Aves #GFP-1020) for visualization of dendrites and 1:3200 rabbit anti-cFos (Cell Signaling 9FG) to validate stimulation. Staining proceeded overnight at 4°C. After 3X PBS washes, respective secondary antibodies were added at 1:1000, washed 3X in PBS, and imaged using Keyence BZ-X710 at 40X magnification. Dendrites were manually traced from the center of the soma using SNT,⁹² with 20-40 neurons collected per replicate where the analyzer was blinded to the condition being analyzed (labeled only by a code by another experimenter). Statistics including Sholl analysis and branch lengths were collected using SNT's Sholl Analysis command and Batch Measure Multiple Files command. Statistics were calculated using GraphPad Prism. Other antibodies used for staining included: Tuj1 (1:2000, Covance MMS-435P, recognizes neuron-specific tubulin).

QUANTIFICATION AND STATISTICAL ANALYSIS

Statistical methods, numbers of biological replicates tested, definitions of significance, tests for comparisons between groups, and descriptions of mean and error plotted are presented in the figure legends. Analyses of genomics and proteomics data is indicated under each Methods subsection.